Range resolution enhancement of WISDOM/ExoMars radar soundings by the Bandwidth Extrapolation technique: Validation and application to field campaign measurements

Nicolas Oudart, Valérie Ciarletti, Alice Le Gall, Marco Mastrogiuseppe, Yann Herve, Wolf-Stefan Benedix, Dirk Plettemeier, Vivien Tranier, Rafik Hassen-Khodja, Christoph Statz, et al.

Range resolution enhancement of WISDOM/ExoMars radar soundings by the Bandwidth Extrapolation technique: validation and application to field campaign measurements

Nicolas Oudart [a], Valérie Ciarletti [a], Alice Le Gall [a, b], Marco Mastrogiuseppe [a,c], Yann Hervé [a], Wolf-Stefan Benedix [d], Dirk Plettemeier [d], Vivien Tranier [a], Rafik Hassen-Khodja [a], Christoph Statz [d], Yun Lu [d]

[a] LATMOS/IPSL, UVSQ Université Paris-Saclay, Sorbonne Université, CNRS, France.

[b] Institut Universitaire de France (IUF), Paris, France.

[c] Sapienza Universita' di Roma, Italy.

[d] Tecnische Universität Dresden, Dresden, Germany.

Abstract

The ExoMars 2022 rover mission has been designed to search for traces of life, past or present, on Mars and more specifically below its hostile surface. This will be the first mission able to collect samples down to 2 meters in the Martian subsurface, where organic molecules and bio-signatures may be preserved. The images of the subsurface (or radargrams) provided by the ground penetrating radar WISDOM onboard the ExoMars rover will be key to select the safest and scientifically most relevant locations for drilling. However, the vertical resolution of WISDOM radargrams is limited (to ~5.5 cm in a typical soil of dielectric constant 4) by the bandwidth of the instrument when applying classical processing techniques. Here we propose to enhance WISDOM radargrams vertical resolution by implementing the Bandwidth Extrapolation (BWE) technique. We demonstrate that this technique yields an improvement of WISDOM vertical resolution by a factor of 3 while well preserving the time of arrival and amplitude of the detected echoes. We validate the BWE technique on synthetic data before applying it to experimental observations acquired both in controlled and natural environments. The resulting super-resolved radargrams greatly improve our understanding of the investigated terrains with a better separation of echoes from underground reflectors, and demonstrate the value of

implementing the BWE technique in the WISDOM data processing pipeline which will ultimately provide images of the Martian subsurface down to a few meters depth with a vertical resolution of ~2 cm in typical soils.

Keywords

Mars; ExoMars; WISDOM; Ground Penetrating Radar; Bandwidth Extrapolation; Resolution;

1. Introduction

In the last decades, radar sounders operated from orbit have opened a third dimension in the exploration of the solar system by revealing the subsurface of a few planetary bodies bringing new clues on their geology and history: the Moon with the Lunar Radar Sounder (LRS) onboard the Kaguya mission (JAXA) (Kobayashi et al., 2012), the nucleus of comet 67/P with the CONSERT radar onboard the Rosetta mission (ESA) (Kofman et al., 1998), and Mars which has been scrutinized by two sounding radars for many years, namely MARSIS onboard Mars Express (ESA) (Picardi et al., 2005) and SHARAD onboard the Mars Reconnaissance Orbiter (MRO/NASA) missions (Seu et al., 2004). In addition, even if not designed as a subsurface sounder, the radar onboard the Cassini spacecraft (NASA/ESA/ASI) (Elachi et al., 2005) has provided insights into Titan's subsurface and in particular the first bathymetry profile of an extra-terrestrial (methane-rich) lake (Mastrogiuseppe et al., 2014). These radars are all operated from orbit and therefore bring clues on the subsurface structure and composition at large scale, with horizontal resolutions typically ranging from a few tens of meters to a few hundred meters, depending on their bandwidth and operating frequencies (Ciarletti, 2016 for a review).

Sounding the subsurface at a much smaller scale to understand the local geological context is possible with ground penetrating radars (GPR) operating from the surface. In 2013, the Chang'E 3 mission carried such a GPR, the Lunar Penetrating Radar (LPR) (Fang et al., 2014), which probed the shallow lunar subsurface (down

to almost 100 m) with a vertical resolution better than 30 cm (Zhan et al., 2014). This pioneer instrument was followed by another LPR onboard Chang'E 4 which investigated the subsurface of the far side of the Moon. Mars will be the next target of on-surface GPRs with two of them to launched in 2020 and to be launched in 2022: the RIMFAX (Radar Imager for Mars' Subsurface Experiment) radar (Hamran et al., 2014) onboard the Mars 2020 (NASA) Perseverance rover, the Subsurface Penetrating Radar (Zhou et al., 2016) onboard the Tianwen-1 rover (CNSA), and the WISDOM (Water Ice Subsurface Deposits On Mars) radar (Ciarletti et al., 2017, 2011) onboard the ExoMars (ESA/ROSCOSMOS) Rosalind Franklin rover. WISDOM has been designed to investigate the subsurface of Oxia Planum down to several meters and with a vertical resolution of a few centimetres, while RIMFAX should be able to probe greater depths (tens of meters) on the Jezero crater region but with a coarser resolution of a few decimetres. The Subsurface Penetrating Radar of the Tianwen-1 mission will perform soundings with a low-frequency and a high-frequency channels, the high-frequency being able to sound the Martian subsurface to a depth of a few meters, with a resolution of a few centimetres. This study is dedicated to the WISDOM GPR selected for the ExoMars rover mission.

ExoMars is an ESA (European Space Agency) / ROSCOSMOS (Russian Space Agency) mission. It will land in 2023 a rover and a surface platform in Oxia Planum, a geologically old plain of Mars (18.3°N 335.4°E), to complement the TGO (Trace Gas Orbiter), in orbit since 2016, which was the first step of the ExoMars program. The main objective of the Rosalind Franklin rover is to seek out traces of past or present life on Mars. Mars being subject to strong radiation levels and oxidation, if such traces still exist, they would likely be in the subsurface (Hassler et al., 2014). To reach them, the rover is equipped with a drill able to collect 3cm-long samples down to 2 meters in the subsurface (Magnani et al., 2010). These samples will be then analysed by a suite of analytical instruments in the rover body (Vago et al., 2017). The selection of safe and scientifically relevant drilling sites requires information on the structure and properties of the Martian subsurface prior to drilling. Two instruments onboard the Rosalind Franklin rover are specifically dedicated to this goal: the neutron spectrometer ADRON-RM (Autonomous Detector of Radiation of Neutrons On-board Rover at Mars) (Mitrofanov et al., 2017) that will provide information about the abundance and distribution of water in the shallow Martian subsurface along the rover path, and the GPR WISDOM.

WISDOM has been designed by the LATMOS (Laboratoire Atmosphères, Milieux, Observations Spatiales, France), the TUD (Tecnische Universtät Dresden, Germany) and the LAB (Laboratoire d'Astrophysique de Bordeaux, France) to unveil the structure and dielectric properties of the Martian subsurface below the ExoMars rover down to a likely maximum depth of ~3 m in a lithic environment with a vertical resolution of a few centimeters. In the context of searching for a drilling place to collect 3-cm long samples (Vago et al., 2017), this latter parameter is key. However, the range resolution of a radar is limited by the instrument bandwidth (2.5 GHz in the case of WISDOM). In this paper, we describe how to expand the nominal bandwidth of WISDOM and therefore to improve the instrument resolution, by implementing in the data processing chain a super-resolution method called the Bandwidth Extrapolation (BWE) technique.

The BWE technique was proposed by the Radar Imaging Technique group of the Lincoln laboratory. The concept was introduced by S. B. Bowling (Bowling, 1977) and then further developed by K. M. Cuomo (Cuomo, 1992) who applied it to radar data. Moore et al. (1997) then applied it to SAR imaging. More recently, the technique has been used to enhance resolution in planetary radar imaging, for example to improve the bathymetric capabilities of the Cassini Radar instrument (Mastrogiuseppe et al., 2014) and the stratigraphic analysis of the Martian polar ice sheets using SHARAD/MRO dataset (Raguso et al., 2018).

Following such promising results, we have adapted and applied the BWE technique to WISDOM data. In this paper, we briefly introduce the instrument and its performances in term of range resolution. Then, we present the BWE technique, and its integration to the WISDOM data processing chain. The method is eventually applied to WISDOM experimental data collected both in controlled, semi-controlled and natural environments.

2. The WISDOM instrument

2.1 The WISDOM ground penetrating radar

WISDOM is the ground penetrating radar mounted onboard the rover of the ExoMars mission (Vago et al., 2017). It is a polarimetric Stepped Frequency Continuous Wave (SFCW) radar operating in the UHF (Ultra

High Frequency) frequency domain and designed to investigate the first meters (typically 3-10 m below the surface) of the Martian subsurface with a centimetric vertical resolution. When performing a sounding, WISDOM transmits and receives a series of N = 1001 harmonic signals of frequencies ν_k between $\nu_{min} = 0.5$ and $\nu_{max} = 3$ GHz separated by a constant frequency step of $\Delta\nu$ = 2.5 MHz.

$$\nu_k = \nu_{min} + (k-1)\Delta\nu \quad (1)$$

Only the real part of the return signal is measured by the instrument, and the complex form is derived via Hilbert transform before applying an Inverse Fast Fourier Transform (IFFT) to obtain the response of the sounded volume. In the time domain, each reflector generates an echo which is characterized by a propagation delay (that can be then converted in distance with assumption on the velocity of the wave in the sounded material) and an amplitude. Since WISDOM antennas are looking downwards at the surface and, while echoes can sometime be generated by off-track reflectors, the retrieved distances are commonly and improperly interpreted as depths. In the following, for the sake of simplification, we represent radargrams in the terms of depth and vertical resolution assuming a value of dielectric constant, rather than range and range resolution.

During operations on Mars in areas of potential interest, WISDOM will acquire soundings every 10 cm along the Rosalind Franklin rover path. These measurements will then be horizontally stacked to form a radar product called “radargram”. A radargram can be regarded as a slice of an image of the subsurface volume, where reflections represent variations in permittivity. In order to ease the Rosalind Franklin rover movements, the WISDOM system has been designed in an air-coupled configuration. The antennas are indeed mounted 38 cm above the ground, which results in the presence of surface echoes in WISDOM radargrams in addition to potential subsurface signals. Lastly, WISDOM has polarimetric capabilities, it can provide radargrams in four polarisation modes (HH, HV, VH, VV) (Plettemeier et al., 2009).

Both WISDOM antennas and electronic unit systems have been calibrated and integrated to the ExoMars rover in 2019. The instrument is expected to be operative on Mars in March 2023, see (Ciarletti et al., 2017) for a detailed description. A data processing pipeline has been developed to automatically generate the radargrams and assist in their interpretation in terms of underground structure and composition (Hervé et al., 2020).

2.2 WISDOM vertical resolution

As previously mentioned, WISDOM is in charge of providing information that will help the mission's scientific team to identify the very layer where to take a sample. In order to achieve this goal, the instrument requires a vertical resolution commensurate with the 3-cm length of the sample.

The range resolution is defined as the shortest distance between two echoes that can be discriminated. In a horizontally layered subsurface, it corresponds to the smallest thickness that can be resolved by the instrument. As previously mentioned, WISDOM is operating in the frequency-domain over a frequency bandwidth B=2.5 GHz and an Inverse Fourier Transform (IFT) is applied to the data to reconstruct the response in time-domain. A radar range resolution δr is limited by the width of the synthetic pulse obtained after IFT, which is inversely proportional to the effective bandwidth of the instrument. In the time domain, two echoes of a same amplitude are commonly considered as resolved if the time delay between them is superior to half the effective pulse width. For a pulse width at -6 dB, in a material having a dielectric constant of ε_r, it follows:

$$\delta r = 1.21 \frac{c}{2B\sqrt{\varepsilon_r}} \quad (2)$$

where c is the speed of light in vacuum (National Instruments Inc., 2009).

Commonly, IFT process involves the use of a window to reduce side-lobe contribution, that could be misinterpreted. With the Hamming window used for this study, the resulting range resolution is degraded to ~1.5 δr. The vertical resolution of WISDOM radargrams in a subsurface with a typical permittivity value of 4 after windowing would therefore become ~5.5 cm which is slightly larger than the desired 3 cm.

Lastly, it is also important to note that the resolution of the radargrams will also be affected by the roughness of the investigated surface and buried interfaces and by scattering due to heterogeneities within the subsurface volume. In addition, because absorption losses often increase with frequency, WISDOM high frequencies (2-3 GHz) are more rapidly attenuated in the medium than smaller ones and the resolution therefore tends to decrease with depth (Hervé et al., 2020).

In the following section, we propose to implement the Bandwidth Extrapolation technique to extrapolate WISDOM spectra to additional frequencies, and therefore obtain a wider bandwidth that would result in an enhanced vertical resolution of the radargrams.

3. Bandwidth Extrapolation technique applied to WISDOM data

3.1 Extrapolation in frequency domain by an autoregressive (AR) linear model

In the frequency domain, a point scatter inside a non-dispersive and lossless sounded volume would generate a sinusoidal signal and the spectrum S resulting from K scatterers is expected to be a sum of sinusoids:

$$S(\nu) = \sum_{k=1}^{K} G_k \exp\left(\frac{-j\,4\,\pi\,\nu\,d_k}{c}\right) \quad (3)$$

where ν is the frequency, d_k the distance between the *k*-th scatterer and the radar, and G_k the amplitude of the return signal from the *k*-th scatterer. As previously explained, a WISDOM sounding consists in a set of spectrum values collected for N discrete frequencies $s_k = S(\nu_k)$ where ν_k is given by equation (1).

This sum of harmonic signals can be modelled by a linear autoregressive all-pole model (Kay and Marple, 1981). Indeed, each sample of the frequency spectrum is the weighted sum of the previous samples for a model in the forward direction (see equation (4.a)) or of the following samples model for a model in the backward direction (see equation (4.b)). If p is the order of the model:

For $p + 1 < n < N$ $$\hat{s}_n{}^f = -\sum_{i=1}^{p} a_i\, s_{n-i} \quad (4.a)$$

and

For $p + 1 < n < N$ $$\hat{s}_n{}^b = -\sum_{i=1}^{p} a_i{}^* s_{n+i-p} \quad (4.b)$$

where $\hat{s}_n$ is the *n*-th sample of the modelled frequency spectrum (indices *f* and *b* corresponding to "forward" and "backward" models), a_i and $a_i{}^*$ the *i*-th coefficient of the model and its complex conjugate, respectively.

For a given order p of the model, the coefficients of the model are determined by minimizing the absolute value of the error between the available samples and their modelled values in the backward and forward directions which are, respectively:

For $p+1 < n < N$ $$e_p^f(n) = s_n - \hat{s}_n{}^f = s_n + \sum_{i=1}^{p} a_i\, s_{n-i} \tag{5.a}$$

and

For $p+1 < n < N$ $$e_p^b(n) = s_{n-p} - \hat{s}_{n-p}{}^b = s_{n-p} + \sum_{i=1}^{p} a_i{}^* s_{n+i-p} \tag{5.b}$$

Therefore, for a frequency spectrum of N samples and a given order p for the model, the total energy E_p of the residual has to be minimized in order to determine the coefficients of the model:

$$E_p = \frac{1}{2} \sum_{n=p+1}^{N} \left(\left| e_p^f(n) \right|^2 + \left| e_p^b(n) \right|^2 \right) \tag{6}$$

This process is known as the "Maximum Entropy Method" (Burg, 1967). It can be implemented using several algorithms, but only the Burg algorithm is considered in this study, as it has proved to guaranty the stability of the model, and performs better on experimental data than the others (Raguso, 2018).

For the best model's order, a value of $p = N/3$ has been experimentally found to yield the best results (Cuomo, 1992; Raguso, 2018) and is commonly used in literature. We will show in section 4.2 that this also applies to the WISDOM dataset.

The idea of the Bandwidth Extrapolation technique is to use the model previously obtained from the available data (i.e., the order p and a_i coefficient values) to extrapolate the spectrum to frequency values outside the initial frequency range. Considering an initial frequency spectrum made of *N* samples, the $(N+1)$-th sample can be estimated in the forward direction:

$$\hat{s}_{N+1}{}^f = -\sum_{i=1}^{p} a_i\, s_{N-i+1} \text{ for frequency } \nu_{N+1} = \nu_{max} + \Delta\nu \tag{7}$$

The same process can be performed in the backward direction,

$$\hat{s}_0{}^b = -\sum_{i=1}^{p} a_i{}^* s_i \text{ for frequency } \nu_0 = \nu_{min} - \Delta\nu$$

leading to negative indices for extrapolation to even lower frequency

$$\hat{s}_{-1}{}^{b} = -\sum_{i=1}^{p} a_i{}^{*} s_{i-p} \text{ for frequency } \nu_{-1} = \nu_{min} - 2\Delta\nu \quad (8)$$

Further estimates are obtained based on the initial dataset gradually extrapolated.

The Burg method (Burg, 1967) is a recursive algorithm which minimizes the value of E_p for increasing values of p. For each order, it calculates the coefficients of the autoregressive linear model with the Levinson-Durbin recursion.

By minimizing the error energy at each iteration, the Burg algorithm ensures that the solution will be stable, all poles of the autoregressive model being within the unit circle. This is an advantage of the Burg method over algorithms such as the Covariance, Modified Covariance and Yule-Walker methods (Kay and Marple, 1981). As previously mentioned, the order of the returned model (the last iteration of p in the algorithm) is an entry of the Burg method.

3.2 Implementation of the Bandwidth Extrapolation technique in WISDOM data processing chain

The data processing pipeline developed for WISDOM is described in (Hervé et al., 2020). Here we briefly recall its main steps and show how it can be completed by the Bandwidth Extrapolation technique.

First, as previously mentioned, WISDOM acquires soundings composed of 1001 real frequency-domain samples. In order to accurately determine the autoregressive model, a Hilbert transform is applied to the real data to convert the signal in complex form. The result is 1001 complex frequency-domain samples. Since the Hilbert transform does not produce any information, the obtained complex data are over-sampled by a factor of two. Therefore, before applying the BWE, following a process recommended in (Kay and Marple, 1981), the data are down sampled by a factor of two. This and has no effect on the range resolution as the bandwidth remains the same. The input soundings in the processing pipeline are thus composed of N= 500 complex frequency samples.

WISDOM data then undergo a temperature correction, followed by a free-space measurement removal to supress constant parasitic signals in radargrams (internal coupling, antenna cross-talk, etc.). A signal whitening or spectrum compensation can be performed by dividing the measured spectra by the instrument transfer function. This transfer function is experimentally obtained from the WISDOM spectrum of an echo

obtained on a perfect reflector (a metallic plate in the case of this study). Because there are several models of the WISDOM antennas and electronic systems (see Hervé et al., 2020), the free-space measurement and the echo on a perfect reflector had to be obtained for each model of the instrument. A DC-offset removal can also be applied to further reduce constant parasitic signals (such as reflections on the rover body).

Then, 5% of the frequency samples are removed on each side of the spectrum, and the Bandwidth Extrapolation technique is applied with an order of $p = N / 3$ for the model (see section 4.2). The removal of 10% of the samples in the spectrum, causing high side-lobes, is part of the Bandwidth Extrapolation technique as described by (Cuomo, 1992). In the case of WISDOM, this effect is caused by the Hilbert transform, which reconstructs better samples near the center than on the edges of the spectrum.

Eventually, windowing is applied to the signal, and a time-domain sounding is obtained after an Inverse Fast Fourier Transform (IFFT) with zero-padding. The signal is extrapolated by a factor of 3, as prescribed by (Cuomo, 1992; Moore et al., 1997). The implementation of the Bandwidth Extrapolation into the WISDOM processing pipeline is illustrated by Figure 1.

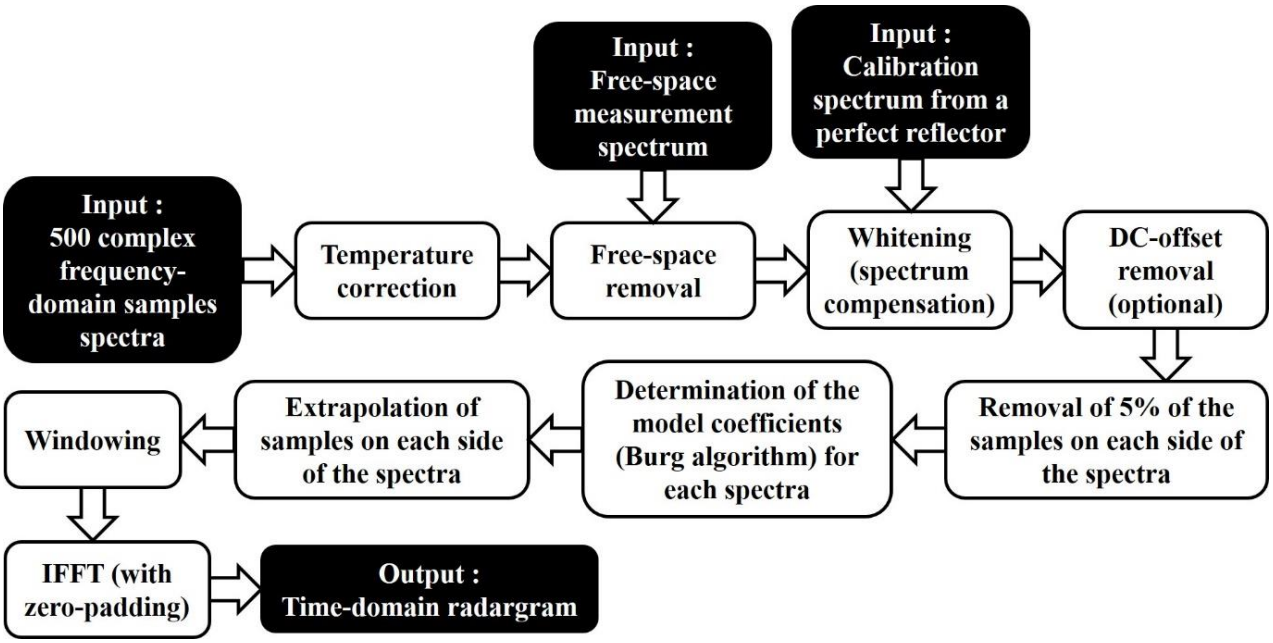

Figure 1: WISDOM processing pipeline including the application of the BWE technique

Additionally, a horizontal interpolation can be employed to ease the interpretation of the radargram. The effect of this last processing is of course purely aesthetic as it does not bring any new information to the radargram.

With this modified processing pipeline, we expect to improve the resolution of WISDOM radargrams by a factor of 3 (the Bandwidth Extrapolation factor). Different tests on synthetic and experimental WISDOM radargrams have been performed to confirm this improvement as further described below.

4. Validation on synthetic WISDOM data

Before testing the Bandwidth Extrapolation on experimental WISDOM soundings, preliminary tests are performed on synthetic data to assert different expected results of the technique.

4.1 Generation of synthetic WISDOM radargrams

Synthetic soundings simulating the presence of two reflectors in vacuum (the worst-case scenario in term of resolution) were generated. For a given distance *d* between the two reflectors, a spectrum between 0.5 and 3 GHz was generated by the addition of two sinusoids of the same amplitude with a phase difference corresponding to twice the distance *d*. A radargram was generated, for *d* values regularly increasing from 0 to 15 cm with a step of 0.25 cm. To some extent, this simulated experiment is similar to what WISDOM should measure over a smooth surface overlying a homogeneous layer getting thicker as the radar moves horizontally above the surface. For sake of realism, an additive white Gaussian noise, resulting in a SNR of 30 dB (in agreement with what is observed on experimental data, see section 5) was applied in the frequency domain. Figure 2.a displays the resulting synthetic radargram (obtained with a Hamming window, zero padding but without BWE). It shows constructive and destructive interference features between the two echoes (that are also observed on the corresponding experimental radargram, Figure 10). The instrument is unable to resolve the echoes when the distance between the reflectors is less than ~11 cm in vacuum, which is consistent with equation (2) for $\varepsilon_r = 1$.

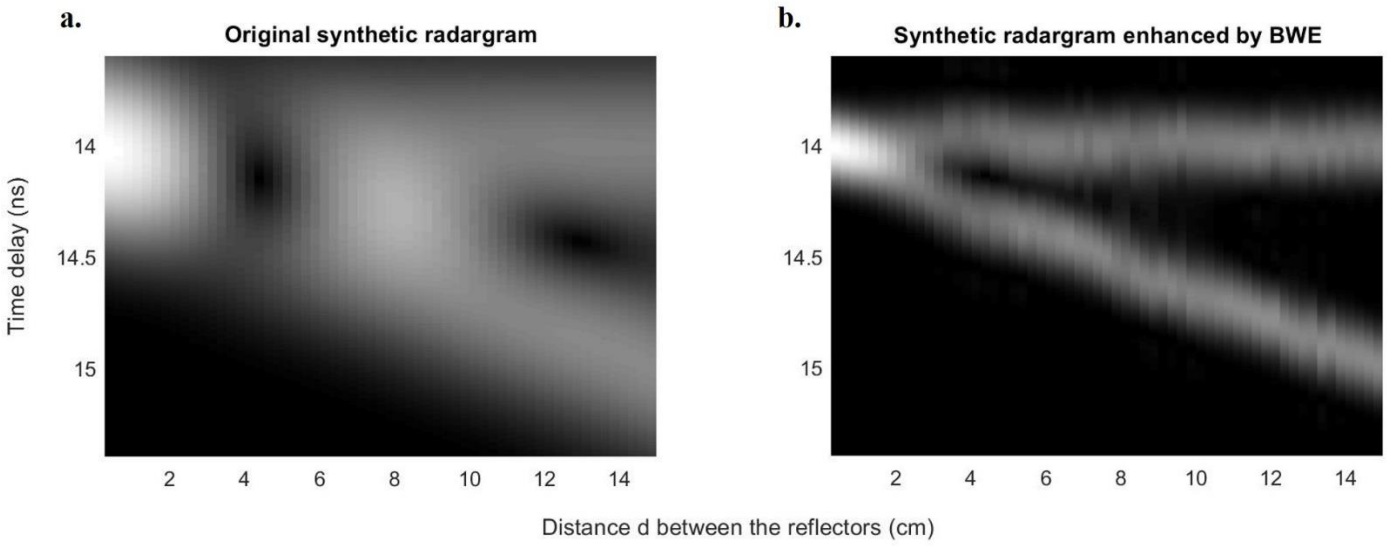

Figure 2: Synthetic WISDOM radargram generated with two echoes and a white Gaussian noise (SNR = 30 dB) a) without BWE b) with BWE.

Figure 2.b displays the radargram that is obtained with the same dataset after BWE to a bandwidth 3 times larger than the original one. As expected, the resolution is improved by a factor 3 therefore reaching ~4 cm (see section 4.3). We will describe in the following how this result has been obtained.

In frequency domain, the accuracy of the BWE applied to this synthetic dataset can also be appreciated. As an instance, Figure 3 presents the application of the BWE to a synthetic sounding generated for d = 15 cm, with the same Bandwidth as WISDOM, and an SNR = 30 dB. As mentioned in section 3.2, first 5% of the samples on each side of the spectrum are removed. Then, the spectrum is extrapolated by a factor of 3. The same sounding has also been generated with three times the Bandwidth of WISDOM but without noise, for the extrapolated samples to be compared to. Figure 3 shows that both the module and phase are well extrapolated by the BWE, leading to a resolution enhanced by a factor of 3 in time domain.

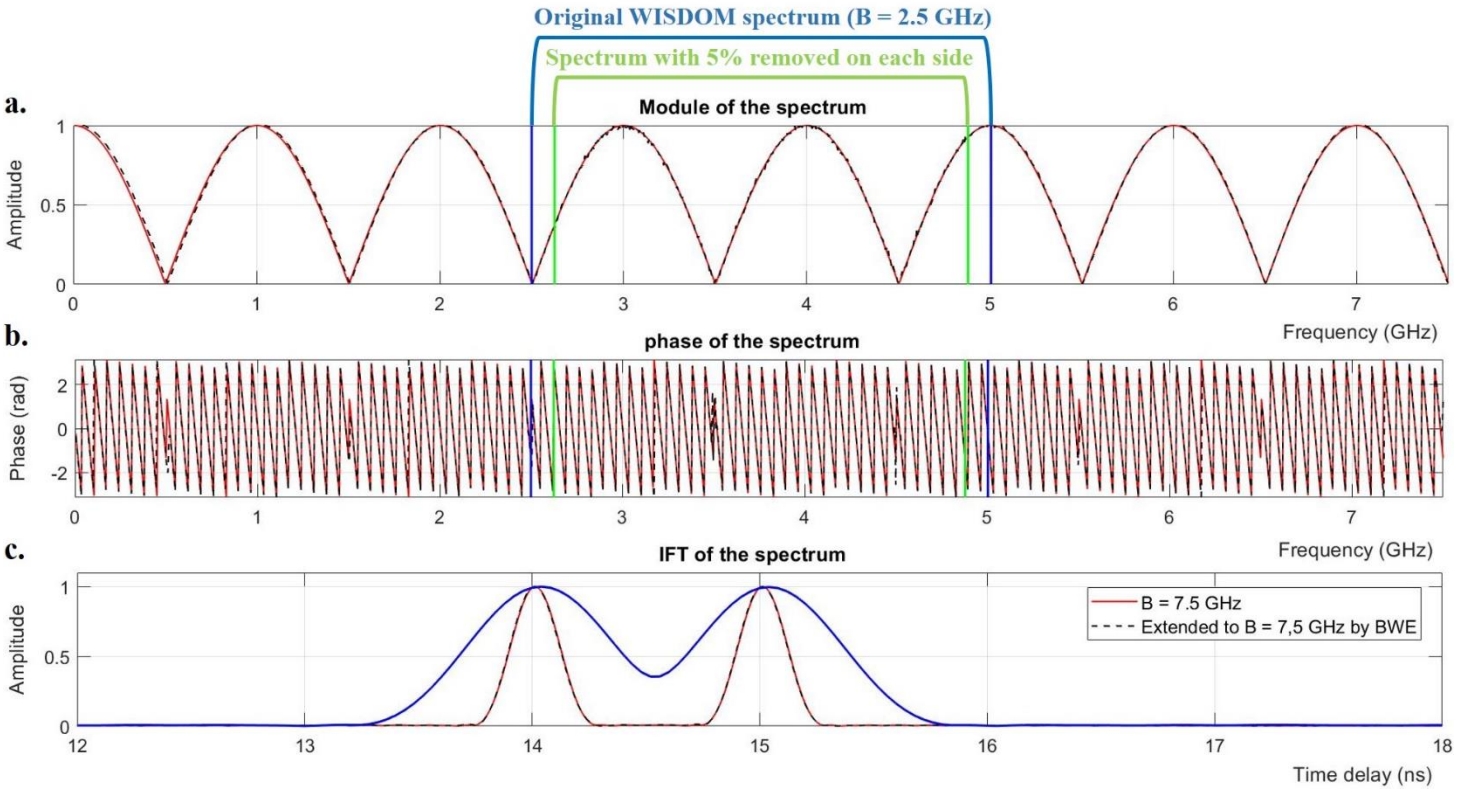

Figure 3: Synthetic spectra (module (a), phase (b)) and corresponding temporal responses obtained by IFT (c), generated for d = 15 cm. The initial spectrum in red is 3 times the bandwidth of WISDOM (7.5 GHz), and the extrapolation by BWE after reduction of this spectrum to the Bandwidth of WISDOM (2.5 GHz) and addition of a white Gaussian noise (SNR = 30 dB) is displayed in dashed black. 5% of the samples are removed on each side of the spectrum before extrapolation.

4.2 Determination of the order of the model

To generate the radargram enhanced by BWE shown in Figure 2.b, we have applied the method described in section 3. The first step of the method is to choose the value for the order p of the autoregressive model. To do that, we limit all the initial spectra to one third of their bandwidth by symmetrically removing frequencies on both sides. Then, we apply the BWE technique to reconstruct the initial dataset for different orders values p ranging from 1 to N. For each p value, the reconstructed radargram is compared to the original one to identify the best order for the BWE algorithm. The correlation between both radargrams is computed, which provides a quantitative analysis of the reliability of the extrapolation. This process is repeated for 1000 noise realisations (Monte Carlo approach). The result is shown in Figure 4.

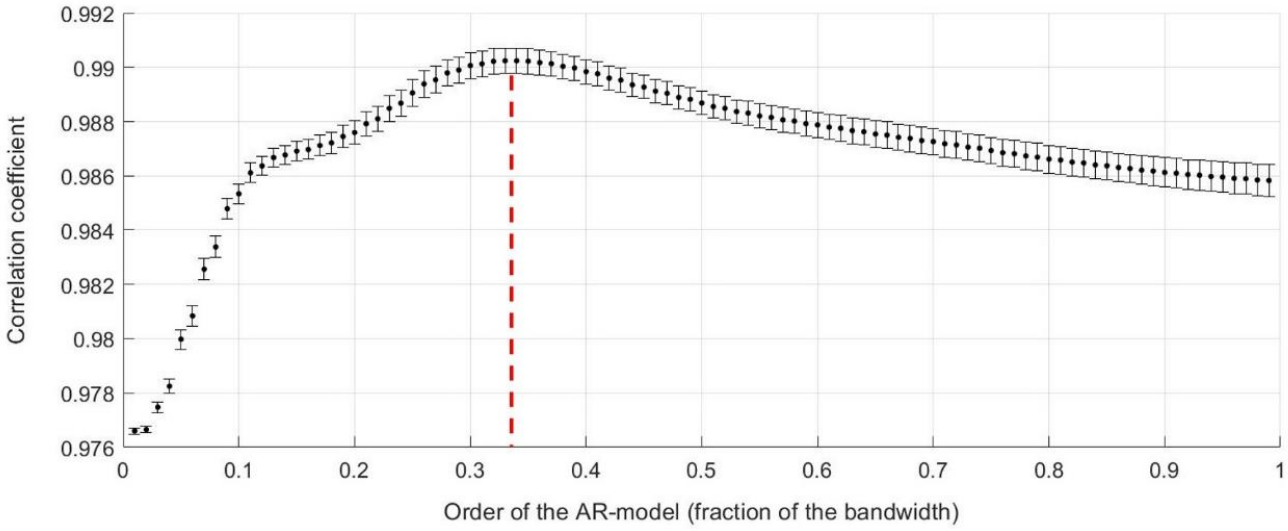

Figure 4: Correlation between a synthetic WISDOM radargram similar to Figure 2, displaying two echoes and white noise (SNR=30 dB) and its reconstruction by BWE after removal of 2/3 of its bandwidth as a function of the order of the autoregressive (AR) model

As can be observed in Figure 4, the correlation coefficient values are high (>0.97) for all p values (which is due to the fact that we only consider 2 reflectors in the case). The highest correlation is obtained for an order of the autoregressive model close to a third of the bandwidth, consistent with the values prescribed in literature. A similar experiment has also been performed by Raguso (2018) on simulated SHARAD soundings, yielding the same result. In the following sections, the order of the model has been therefore set to $p = N / 3$.

4.3 Effect of the BWE on the resolution

With the same dataset, it is possible, from the time delays measured at the peaks of the two echoes (when resolved), to obtain an estimate of the distance between the two reflectors and to compare this estimate $\hat{d}$ to the known distance d in order to test the ability of BWE to improve the resolution of the soundings. In Figure 5, the mean value of the error $\hat{d} - d$, with its standard deviation computed on 1000 realisations (Monte Carlo approach) a randomised phase for the first echo is displayed as a function of d.

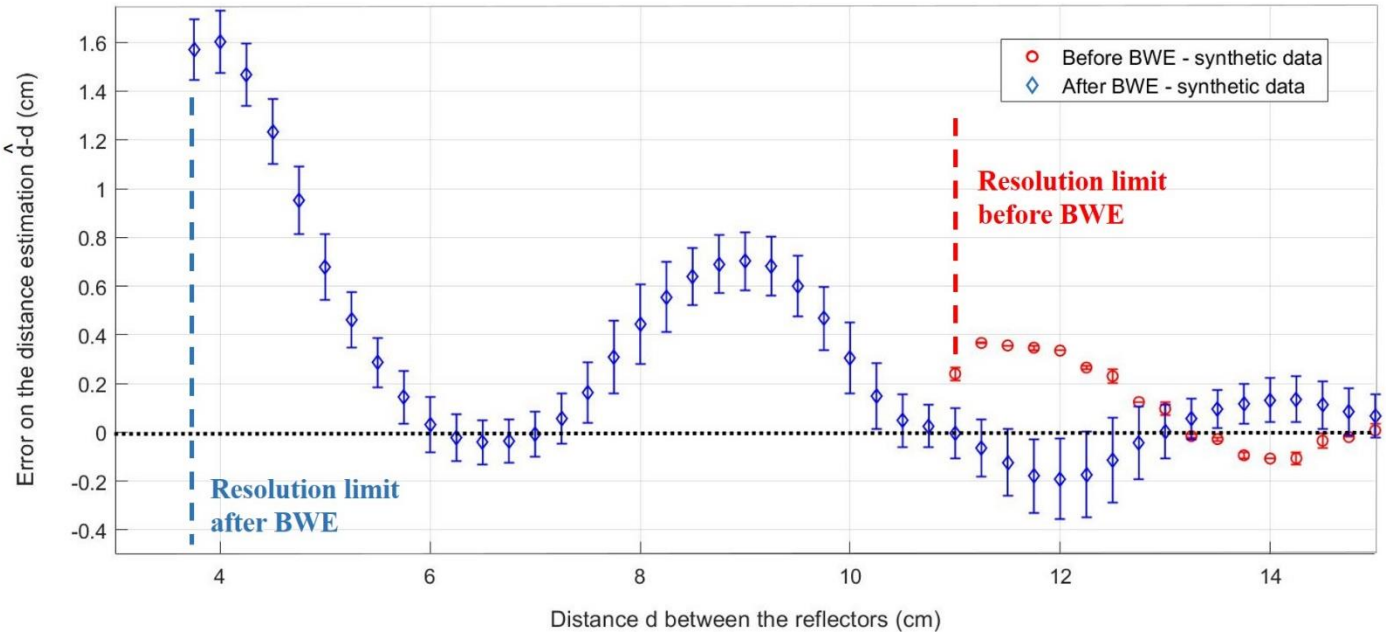

Figure 5: Error on the estimation of the distance between two reflectors generating synthetic echoes of the same amplitude as a function of the distance between these reflectors. 1000 synthetic cases with a Gaussian noise such as SNR = 30 dB have been considered; the first echo has a random phase.

Without BWE, the simulated echoes obtained with $d < 11$ cm cannot be separated, while with BWE this limit is brought to 3.75 cm with an error that remains well below the expected resolution.

It can be also noted that, with or without BWE, the error oscillates, depending on the phase between the two echoes. Further, the error decreases as d increases. For the considered d values, it lies between -0.2±0.15 and 1.6±0.13 cm. The amplitude of the oscillation is higher after the application of the BWE due to the sensitivity of the Burg algorithm to both phase and noise, as already depicted by Kay and Marple (1981).

Synthetic radargrams have also been generated for media other than vacuum i.e., with higher dielectric constants; they show that the amplitude of the oscillation decreases as the dielectric constant increases, the error always remaining below the expected resolution.

4.4 Effect of the BWE on the precision

Having studied the effect of the BWE on the resolution with the generated synthetic dataset, it is also important to verify that this technique does not alter the positions of the reflectors. In other words, that the precision of

the super-resolved radargrams remain barely changed after application of the BWE. For each echo, the error on the estimation of its position is measured for each value of d before and after application of the BWE.

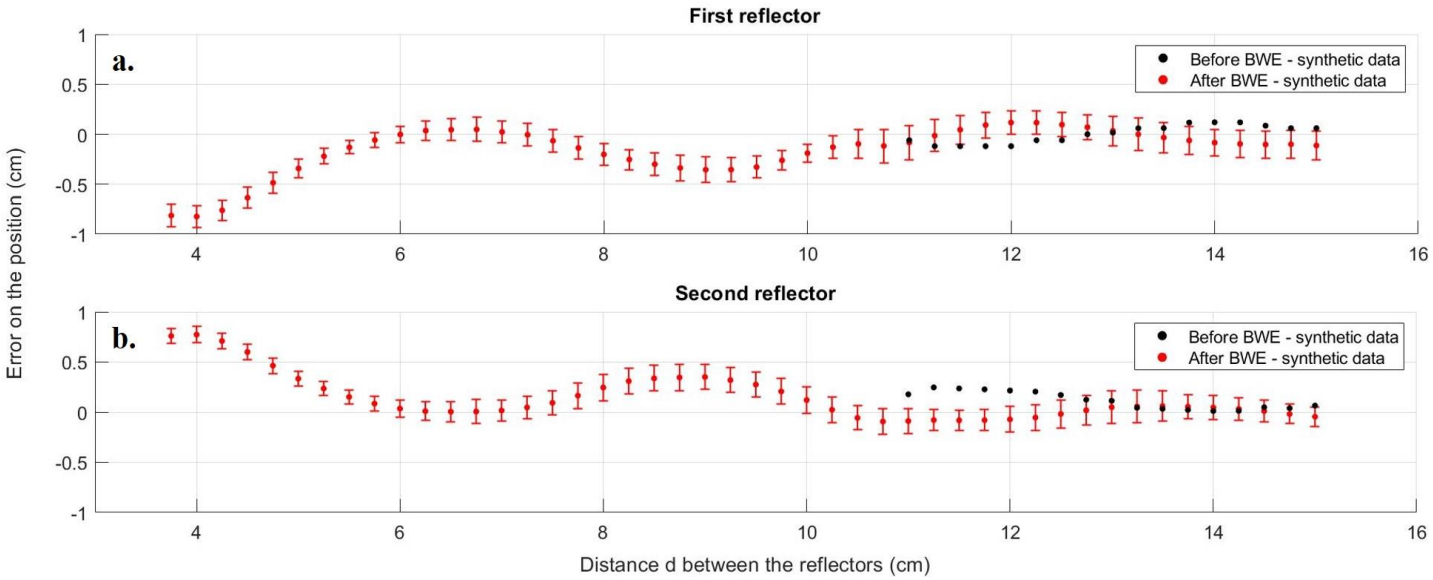

Figure 6 Error on the position of the synthetic echoes before and after application of the BWE (Figure 2) as a function of the distance d between these reflectors. 1000 synthetic cases with a Gaussian noise such as SNR = 30 dB have been considered. The first echo has a random phase.

Figure 6 displays the error on the position of both echoes as a function of *d*. It can be observed that the absolute error on the position stays below 1 cm as it oscillates. It is even lower than 0.5 cm for d > 5 cm. This worst case result (i.e., in vacuum) demonstrate the ability of the BWE to increase the resolution of the WISDOM soundings without impairing their precision.

A precision of 1 cm on the position of an underground layer is three times lower than the length of the sample to be collected by the mission drill. This result is therefore satisfactory, allowing to aim at a precise underground interface without the risk of missing it.

4.5 Effect of the BWE on the echo amplitude

An advantage of the BWE, when compared to other super-resolution techniques (MUSIC, ESPRIT), is the conservation of the amplitude of each echo in the enhanced radargram (Cuomo, 1992). This advantage is

essential because, in experimental data, the echo amplitude will ultimately be used to infer information about the reflecting structures (starting with the permittivity value in a case of a smooth interface). The ability to obtain a satisfactory estimate of the amplitude has been tested on the previously described synthetic dataset for which the amplitude of both echoes has been set to 1. When these latter ones are resolved by BWE (i.e., for d > 3.75 cm after BWE), the ratio between the first echo amplitude and the second echo one is computed. Figure 7 shows the mean value of this ratio with the corresponding standard deviation as a function of d.

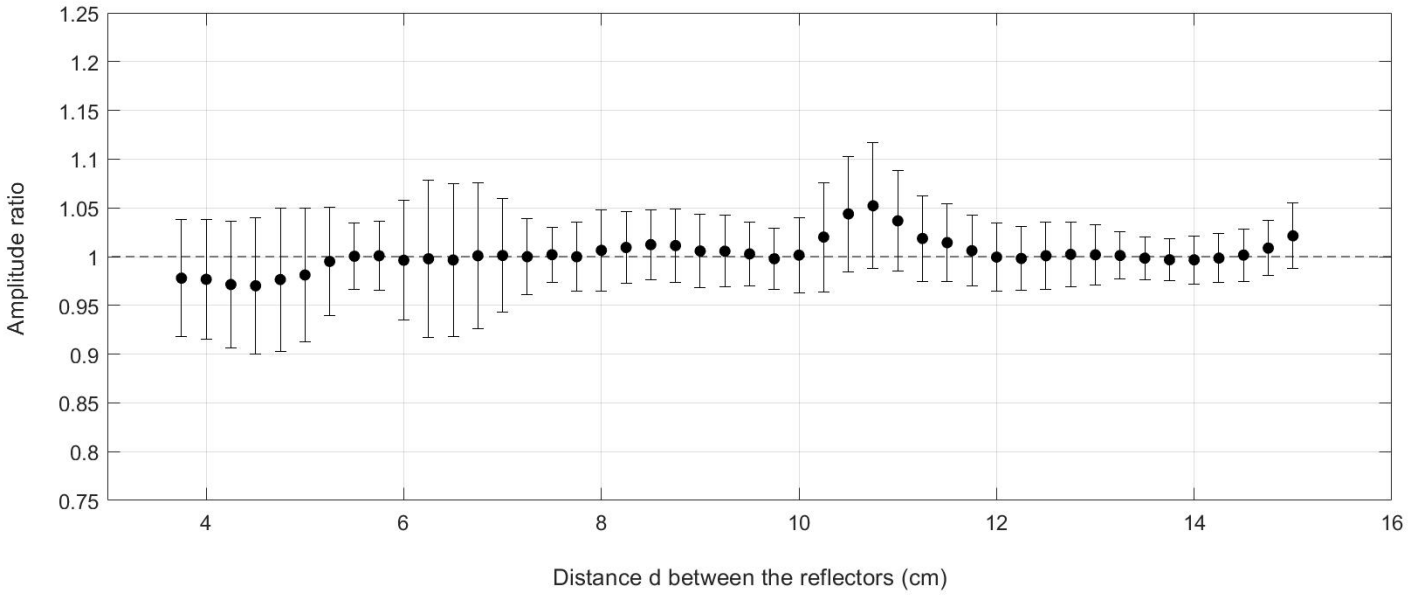

Figure 7: Amplitude ratio measured between two synthetic echoes after application of the BWE (Figure 2.b) as a function of the distance d between these reflectors. 1000 synthetic cases with a Gaussian noise such as SNR = 30 dB have been considered. The first echo has a random phase. The echoes have been initially generated with the same amplitude (Figure 2.a) so that the expected amplitude ratio is 1.

By construction the amplitude ratio between echoes is 1 and, after BWE, its mean value remains within between 0.97 and 1.05 with a standard deviation of about 1.6%, which is very satisfactory. On data collected in a natural environment corresponding to a similar configuration (that is a smooth surface on the top of a layer having an increasing thickness along the radar displacement) the measurement of such a ratio would provide an estimate of the losses in the uppermost layer, thus bringing information on the loss tangent (ratio

between the imaginary and real parts of the permittivity) and/or on the heterogeneities embedded within this layer. For example, considering the case of a homogeneous layer with a typical dielectric constant 4 and loss tangent 0.03, over a layer of dielectric constant 6 with smooth interfaces, and soundings for distances ranging from 3 to 15 cm with a step of 0.25 cm, an error with a standard deviation of 5% on the ratio estimate would result in an error on the loss tangent with a standard deviation of 3% (Monte-Carlo with 100000 cases) according to the model proposed by Picardi et al. (2008).

The derivation of the loss tangent and, overall, a better understanding of the composition of the investigated terrains require to know the dielectric constant of the uppermost layer. This later, especially if the surface is smooth, can be derived from the amplitude of the surface (first) echo (Hervé et al., 2020) which, as shown below, is also well preserved after application of the BWE.

Figure 8 displays amplitude of the first (Figure 8.a) and the second echo (Figure 8.b) extracted from Figure 2.b after application of the BWE. The amplitude of the two synthetic echoes was initially set to 1 and remains close to unity after BWE. We further note that both echoes present similar variations in amplitude, with oscillations that are once again clearly correlated to the phase between the echoes.

For distance values d > 9.5 cm in vacuum (i.e., 4.75 cm in a medium with a typical dielectric constant of 4), the error on the amplitude of the first echo (corresponding to the surface echo) is less than 2.5% (see Figure 8.a). As an illustration, such an error on the surface echo amplitude would lead to an error on the retrieval of the permittivity of the top layer of less than 4% for a permittivity value of 4. This would result in an error in distance estimate of less than 2 cm at a depth of 1 meter. For d > 5 cm (i.e., 2 cm with the same hypothesis as above), the error on the first echo being less than 7%, the error at 1 m depth would be ~5.2 cm.

This same error on the amplitude estimate would also translate in an error on the material's porosity retrieval. In fact, assuming an a priori knowledge on the composition of a Martian soil, its porosity can also be derived from the real part of the permittivity. For instance, according to the model experimentally determined by Brouet et al. (2019), at 0.5 GHz and 200 K the dielectric constant is linked to the porosity ϕ by $\varepsilon \approx (12.03 + 2.1)^{1-\phi} - 0.043$, and at 3 GHz by $\varepsilon \approx (8.87 + 2.05)^{1-\phi} - 0.043$ for pure JSC Mars-1 Martian simulant. In the first case (0.5 GHz), for a measured dielectric constant of 4, the error on the estimation of

porosity would be ~5.7%. In the second case (3 GHz), the error would be ~7.2%. In both cases, a satisfying low level of error.

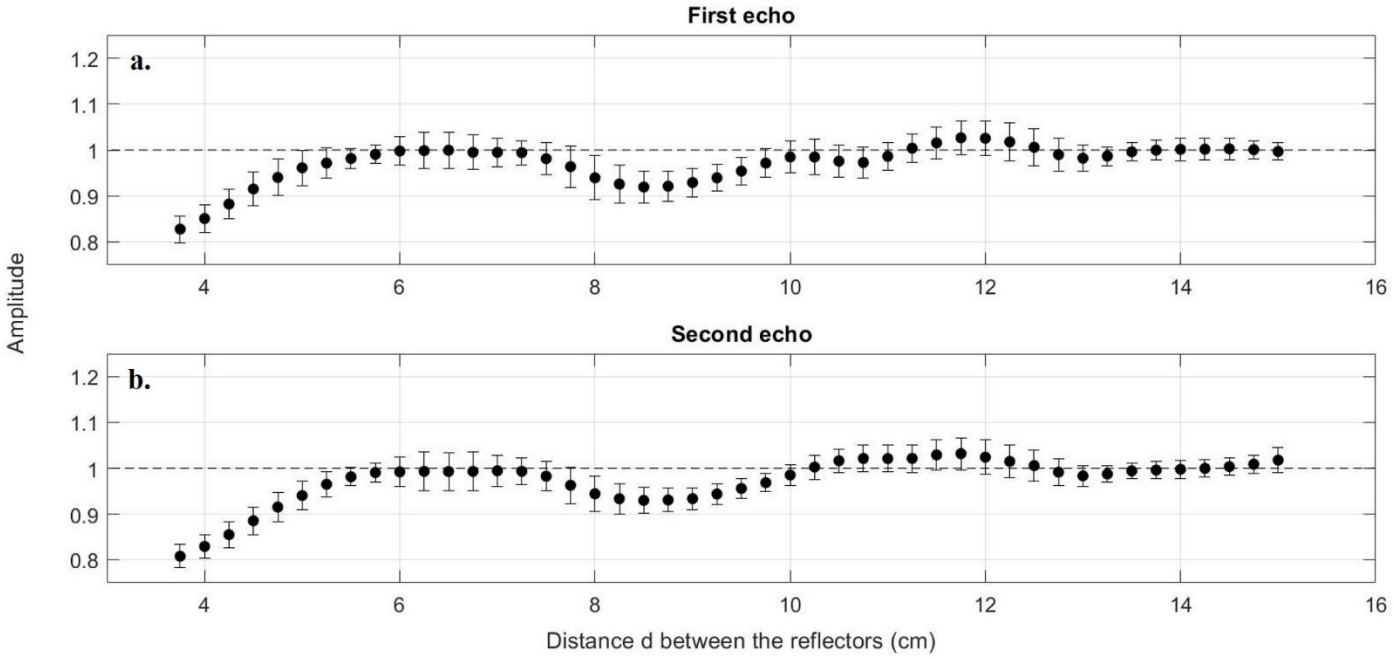

Figure 8: Amplitudes of the first (a) and second (b) synthetic echoes after application of the BWE (Figure 2b) as a function of the distance d between the two reflectors. 1000 synthetic cases with a Gaussian noise such as SNR = 30 dB have been considered. The first echo has a random phase. Both echoes have been initially generated with an amplitude of 1 (Figure 2.a) and this amplitude is well preserved after BWE although some oscillations appear due to phase differences between the echoes.

These different tests validate on synthetic data the ability of BWE to improve by a factor of 3 the vertical resolution of WISDOM radargrams. We have also demonstrated that the distance between reflectors and the amplitude of the echoes are well preserved by this technique and can therefore be used to characterize the surface and subsurface. In the following, the method is applied to experimental WISDOM data collected in controlled environments to further confirm the value of the BWE technique.

5. Validation of the vertical resolution improvement on experimental data

5.1 Application of the Bandwidth Extrapolation technique to WISDOM "two reflectors" laboratory experiment

In order to validate the gain in resolution brought by the BWE technique on experimental data, we have performed laboratory measurements, at LATMOS, with the spare model of the instrument, in configurations as close as possible to the simulated "two reflectors" case described in Section 4. Two metallic plates were placed side by side in front of WISDOM antennas and separated by a varying distance *d* (Figure 9*)*. More specifically, the first metallic plate remained at the same distance from the antennas (~42.6 cm) while the second one was progressively moved away from 1 to 14 cm by steps of about 1 cm.

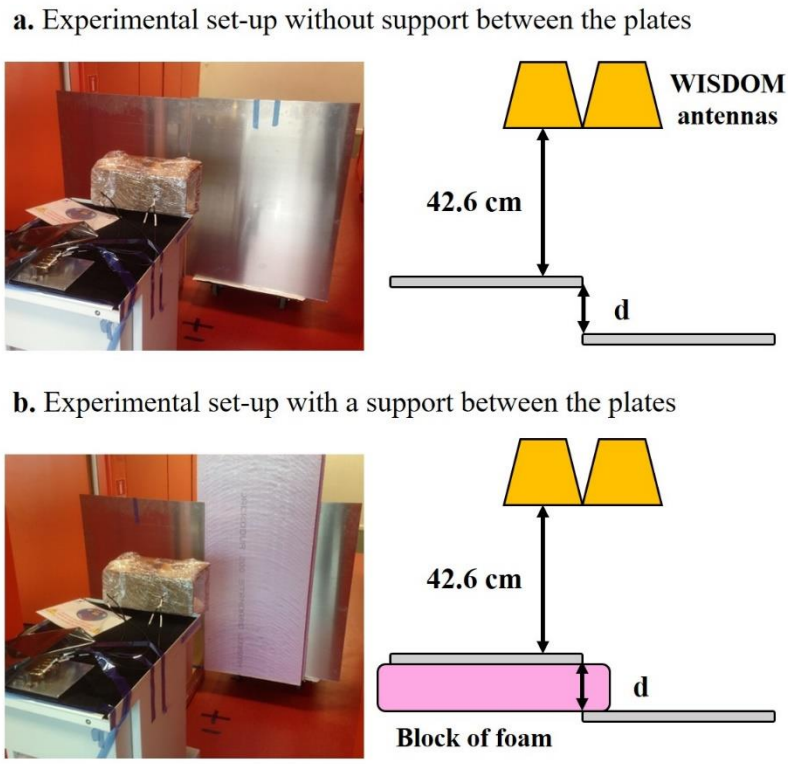

Figure 9: Illustrations of the experimental set-up for the "two reflectors" experiment performed at LATMOS. a. Experimental set-up without support between the plates b. Experimental set-up with a support between the plate.

411 The resulting WISDOM radargram (Figure 10.a to be compared to Figure 2.a) shows echoes from the two
412 plates but also undesired reflections (at the corners of the metallic plates for instance) and constructive and
413 destructive interferences due to the superposition of the two echoes from the plates. This radargram has been
414 processed as described in Section 3.3 with the following exception: no DC-offset removal has been performed,
415 because it would have suppressed the echoes from the first metallic plate (which displays a constant arrival
416 time and amplitude).

417 The measurement error on distance *d* is estimated to be around 0.2 cm (measurements were performed with a
418 graduated ruler). In order to reduce the measurement uncertainty some of the soundings were performed with
419 polystyrene foam plates of known thicknesses (instead of air) between the metallic plates (see Figure 9.b); this
420 ensures a more accurate positioning of the metallic plates. Polystyrene foam is nearly transparent to radio
421 wavelengths and has a permittivity value close to 1, such a set-up therefore remains close to a "two reflectors"
422 case. In the following, measurements performed with a polystyrene foam support will be highlighted.

423 Comparison between Figure 10.a and Figure 2.a reveals that simulated and experimental data present the same
424 behaviour except that the second echo is weaker than the first one in experimental data. In particular, we note
425 that the constructive and destructive interferences are very similar in these datasets. Both original radargrams
426 show that, with conventional processing, it is impossible to confidently separate echoes when the distance
427 between the reflectors is smaller than 11-12 cm. This is consistent with the expected theoretical vertical
428 resolution after windowing (~11 cm in vacuum using equation (1) and 1.5 δr, section 2). After application of
429 BWE (Figure 2.b and Figure 10.b), the echoes are resolved down to a distance between 3 and 4 cm which
430 translates into a resolution improvement by a factor ~3.

431

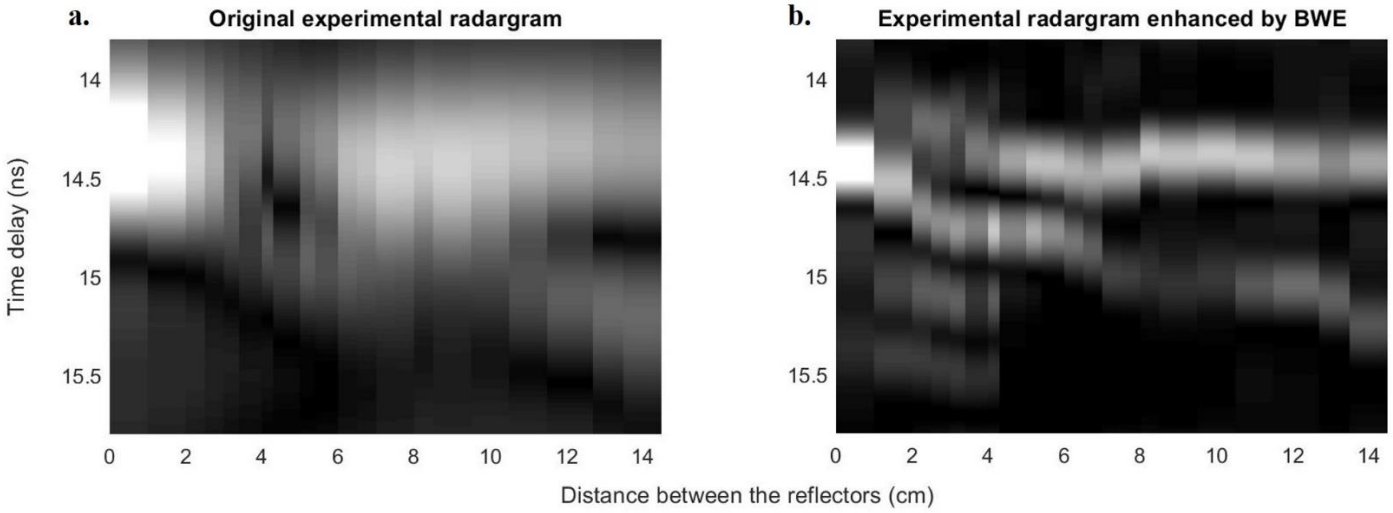

Figure 10: Experimental radargram before (a) and after (b) application of the BWE.

Figure 11 shows two examples of experimental soundings obtained for the specific cases of d = 6 cm (Figure 11.a) and d = 10.5 cm (Figure 11.b). In Figure 11.a, the distance of 6 cm is well below the resolution expected in vacuum with common spectral processing techniques and windowing according to the criterion defined in section 2.2. After application of the BWE, the two echoes are clearly resolved, and their pulse width is significantly reduced which gives a further illustration of the benefit of this technique. The distance between the two reflectors is only slightly underestimated by ~0.37cm. The amplitude of the first echo before BWE is higher than the amplitude of each echo after BWE, which can be explained by the fact that before BWE the two echoes are interfering.

In Figure 11.b, the distance of 10.5 cm is still slightly below the resolution according to the criterion defined in section 2.2. In fact, the presence of two echoes can already be noticed before BWE, but they still interfere strongly. The application of the BWE once again reducing the pulses widths makes the echoes more clearly resolved. The error on the estimated distance between the reflectors is ~0.94cm. Because of the interference between the two echoes, the difference in amplitude before and after resolution enhancement is not unexpected.

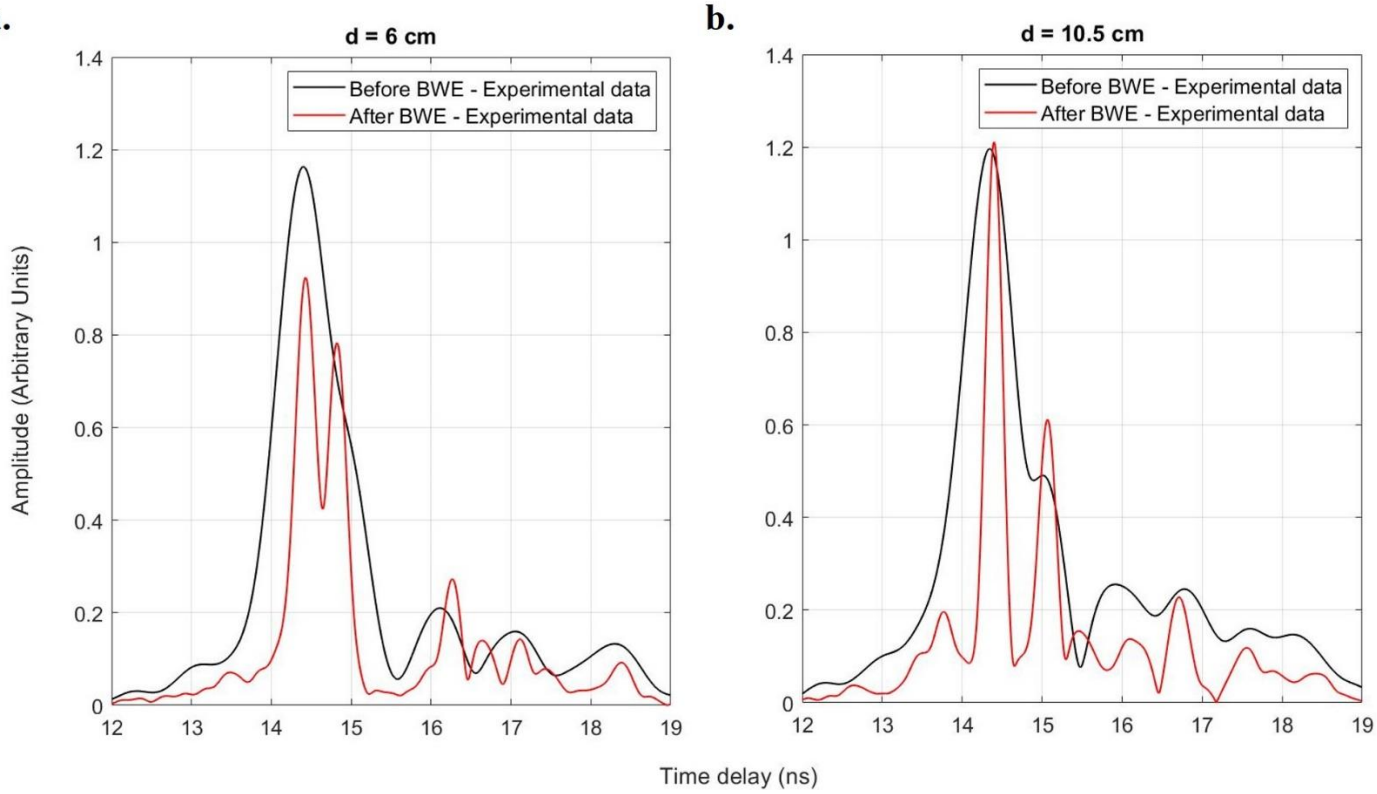

Figure 11: Experimental WISDOM soundings before and after application of the BWE for distances of 6 cm (a) and 10.5 cm (b) between the two reflectors

5.2 Distance estimation after application of the BWE

A peak detection can easily be applied to the different soundings performed without and with BWE to measure the time delay between the two echoes coming from the metallic plates and therefore the distance between these plates, as performed in Section 4 on synthetic soundings. Figure 12 shows the error on the estimated distance as extracted both from the synthetic and the experimental datasets and before and after BWE.

As previously mentioned, for the synthetic data, each sounding has been generated with 1000 cases of noise, with a SNR = 30 dB. Mean values of the distance error with associated standard deviations are displayed in Figure 12 as a function of the distance between the reflectors. For the experimental data, only one measurement is performed for a given distance *d* which has been measured with an uncertainty of about 0.2 cm. This uncertainty on the distance between the metallic plates leads to the same uncertainty on the error

462 between the distance and its estimation. Soundings performed with a foam support between the two metallic
463 plates are indicated by an arrow.

464

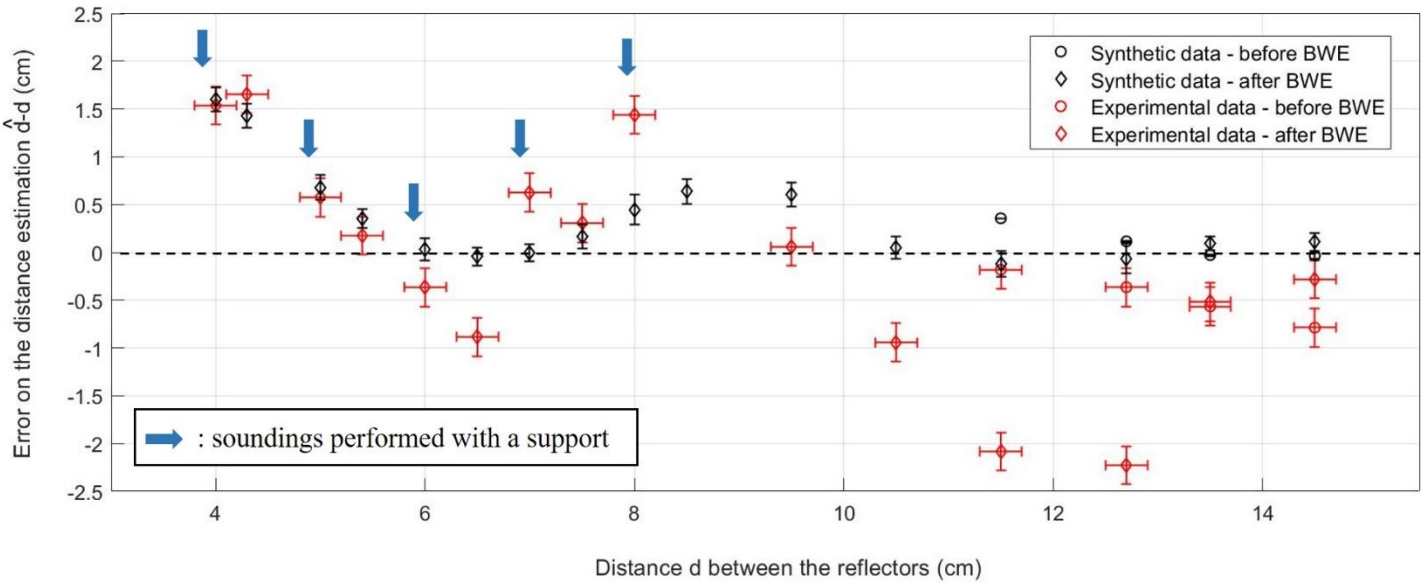

465

466 *Figure 12: Error on the distance estimation between the reflectors before and after application of the BWE*
467 *as a function of d for both synthetic (1000 cases of noise with SNR = 30 dB) and experimental sounding.*

468

469 On simulated and experimental data, the BWE significantly improves the resolution which is enhanced to 4
470 cm compared to 11 cm without BWE, i.e. by a factor close to 3. The oscillations in the measured distance
471 error, already noticed on synthetic data (Figure 5), are also clearly visible on the experimental data, with and
472 without BWE. As mentioned in section 4, their presence is due the phase difference between the two echoes
473 (Raguso, 2018).

474 We further note a good match between the errors measured on synthetic and experimental data for distances
475 smaller than 10 cm. For greater distances, while the test on synthetic data predicts a diminution of the
476 oscillations, such diminution is not observed on experimental results and the error is actually slightly smaller
477 without BWE (< 1.55 cm). However, the maximum absolute error after BWE is ~2 cm which remains below
478 the desired vertical resolution.

As a conclusion, the present experiment demonstrates that an improvement in resolution by a factor of 3 in WISDOM radargrams can be achieved thanks to BWE. The reached resolution is 4 cm in vacuum with an error on the estimated distance < ~2 cm. Both the vertical resolution and error would be even smaller in media with a dielectric constant > 1.

From this experiment, unlike on synthetic data in section 4, the error on the amplitude of each echo cannot be drawn. The synthetic data were indeed generated with an amplitude we fixed for each echo while the echo amplitude is not known for experimental data. The only comment possible here is that for soundings where the two echoes are resolved both before and after BWE, amplitudes are quite close. The differences are likely due to interferences, which are still present for distances near the resolution limit.

The experiment described in this section has also been performed with experimental soundings obtained in an anechoic chamber on a single plate. The soundings have been modified to simulate a delay in time domain and added in order obtain two echoes. The results are very similar to the experimental results shown in this section.

In the following, the BWE is applied to WISDOM experimental radagrams acquired during field tests performed on different types of environments.

6. Application of the Bandwidth Extrapolation technique to WISDOM field test data

Between 2010 and 2019, several field campaigns have been organised in order to evaluate WISDOM performances on different environments, some of them potentially analogs to the Martian subsurface. These field tests have been performed with various models of the instrument, the first ones with prototypes and the most recent ones with models similar to the instrument flight model. The result is a large dataset of radargrams to which BWE can be applied.

We have selected four campaigns, during which structures of interest were detected in the subsurface, and for which the application of the BWE proved to be very helpful for radargram legibility and interpretation. For some campaigns, no free-space or no calibration measurements are available. When no free-space is available, only a DC-offset removal is applied to the signal. When no calibration is available, the surface echo is used for the whitening process (see section 3.3).

Table 1 The different field tests selected for this study

Campaign location	Year	Type of environment	Free-space and calibration	Model of the instrument
Etna (Italy)	2010	Lithic (volcanic)	Calibration measurement No free-space measurement	Prototype
Chamonix (France)	2011	Icy (snow and ice layers)	No free-space measurement No calibration measurement	Prototype
Dachstein Giant Ice Cave (Austria)	2012	Icy (ice with a bedrock and trapped boulders)	Calibration measurement No free-space measurement	Prototype
Dresden TU (Germany)	2019	Semi-controlled environment (reflectors buried in a soil trench)	Free-space measurement Calibration measurement	Copy of the Flight model

The different field tests are briefly described in Table 1. In the following, a radargram from the semi-controlled environment will be presented, then the radargrams from icy environments, and lastly a radargram from a lithic environment.

6.1. Semi-controlled environment: The Dresden "Mars Yard" campaign

In June 2019, a measurement campaign took place in the Technische Universität of Dresden (TUD, Germany) facilities with a copy of the instrument flight model (electronic unit and antennas). Free-space measurements and calibrations on metallic plates were performed in an anechoic chamber. WISDOM acquisitions were performed across a 75 cm deep soil trench, where different reflectors were buried. This type of campaign is important to validate the interpretation of WISDOM radargrams, as the reflectors locations are known prior to the acquisition.

One of the experiments performed during this measurement campaign is called the "metallic staircase" experiment. Seven blocks of concrete wrapped in aluminium foils were organized to form a staircase (see Figure 13). Regularly spaced WISDOM soundings were performed above the staircase, with a step of 5 cm. The resulting radargram is shown on Figure 14.a. It displays clear scattering patterns but because each step of the staircase had a height of 10 cm, they are barely resolvable in the air without BWE.

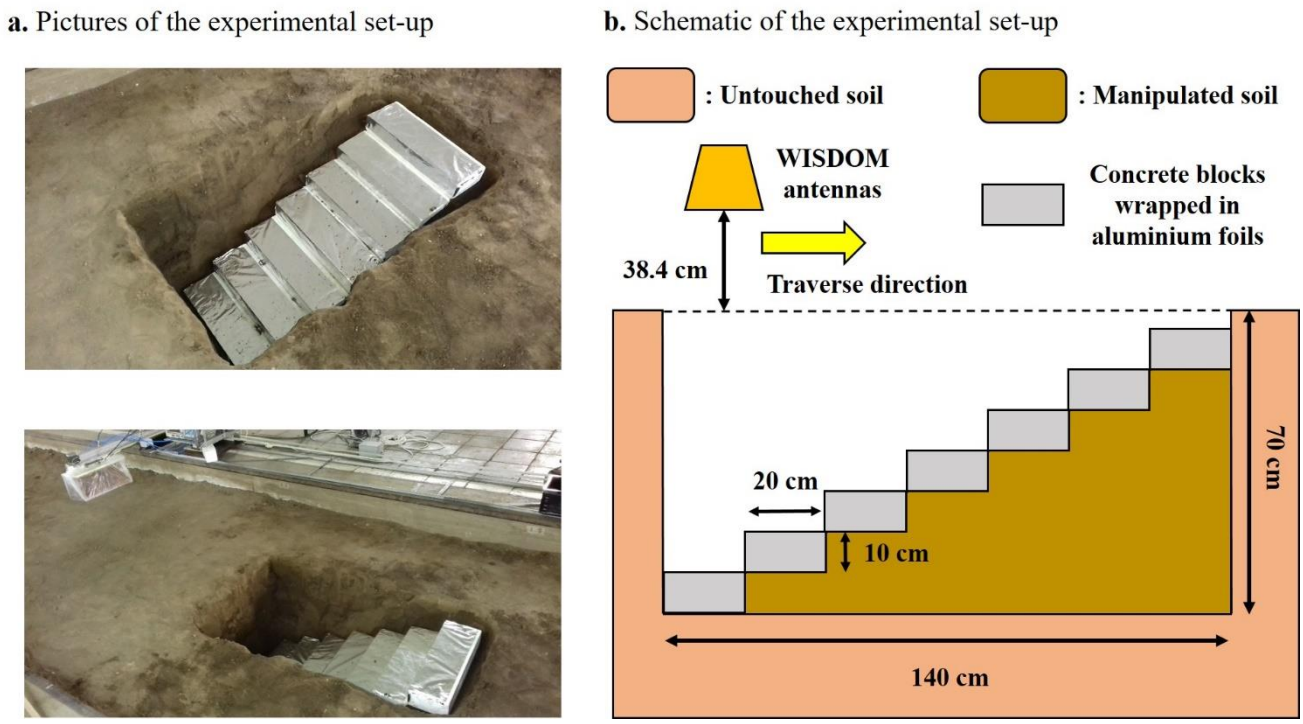

Figure 13: Illustration of the TUD experimental set-up for the "metallic staircase" experiment

First, as a further test of the BWE value, the soundings acquired on the metallic staircase have been reduced in bandwidth: a third of the frequencies were removed on each side of the spectra (Figure 14.b) before being reconstructed by BWE (Figure 14.c). In the original radargram (Figure 14.a) obtained without BWE, even if the echoes from two successive steps are not vertically resolved, they can be located thanks to the horizontal variations as the radar moves at the surface. After reduction of the bandwidth (Figure 14.b), the resolution is drastically coarser and identifying the staircase is very challenging. After reconstruction by BWE (Figure 14.c), individual step can be located anew. Comparison between (Figure 14.a) and (Figure 14.c) demonstrates the accuracy of the reconstruction by BWE and that the technique does not introduce artefacts. The SNR after

reconstruction by BWE also seems higher, which is expected as the AR models are determined by the Burg algorithm with an order corresponding to a third of the bandwidth, meaning that soundings are extrapolated accounting for a large portion of previous/following samples, and thus reducing the effect of noise from the bandwidth reduced signal in the reconstruction.

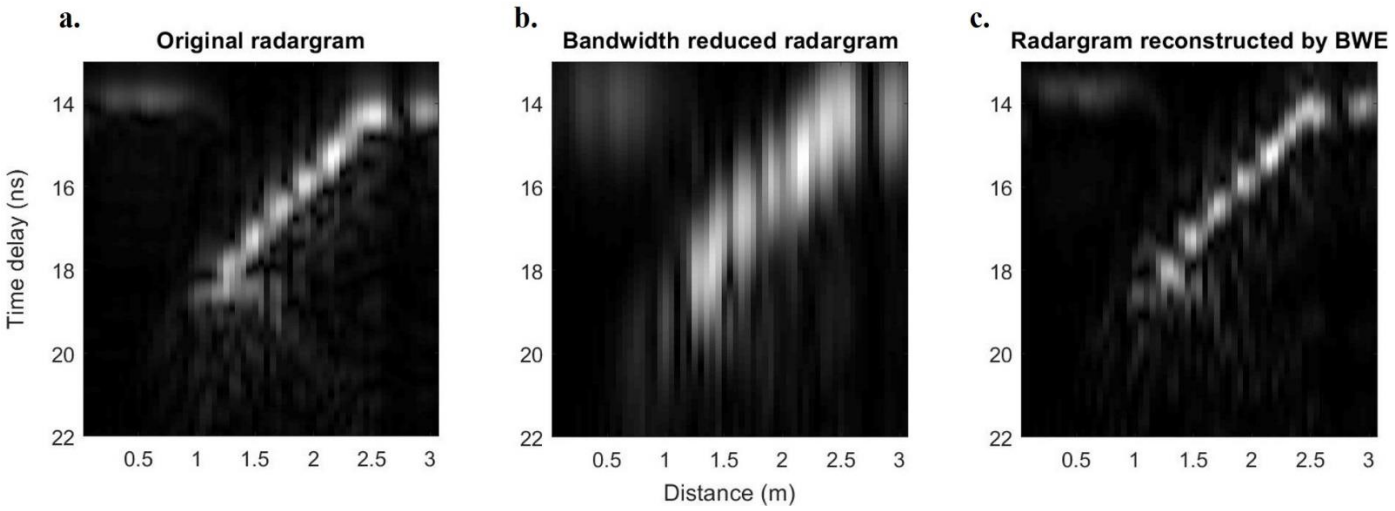

Figure 14: TUD "staircase" radargram as acquired (a), after reduction of the bandwidth by removing one third of the frequencies (b), and after reconstruction by BWE (c).

The BWE was then applied to the original radargram (Figure 14.a) and the resulting radargram is shown in Figure 15. The surface echo from the borders of the hole is more clearly detected (arrow 1 in Figure 15.b). As expected, the steps can now be clearly separated. The staircase being in the air, the distance can easily be estimated from the time delay. The vertical separation of 10 cm between each step, and their horizontal extension of 20 cm are retrieved. Hyperbolic branches corresponding to diffraction effects at the corners of the steps are revealed (arrow 2), even if, due to the geometry of the metallic staircase, only the left branch of the hyperbolic shapes is visible. These hyperbolic branches appear here because the improvement in resolution reduces the effect of interferences between them, which explains why the hyperbolic branches cannot be seen before BWE.

Being able to detect these hyperbolic shapes is very important because they are commonly used to estimate the averaged permittivity of the medium separating the antennas from the reflecting structures (Daniels, 2005).

We applied a Hough transform (Capineri et al., 1998) to the region of the deepest hyperbolic shape, and derived a dielectric constant of 1.0±0.1 consistent with a scatter in the air (see Figure 15).

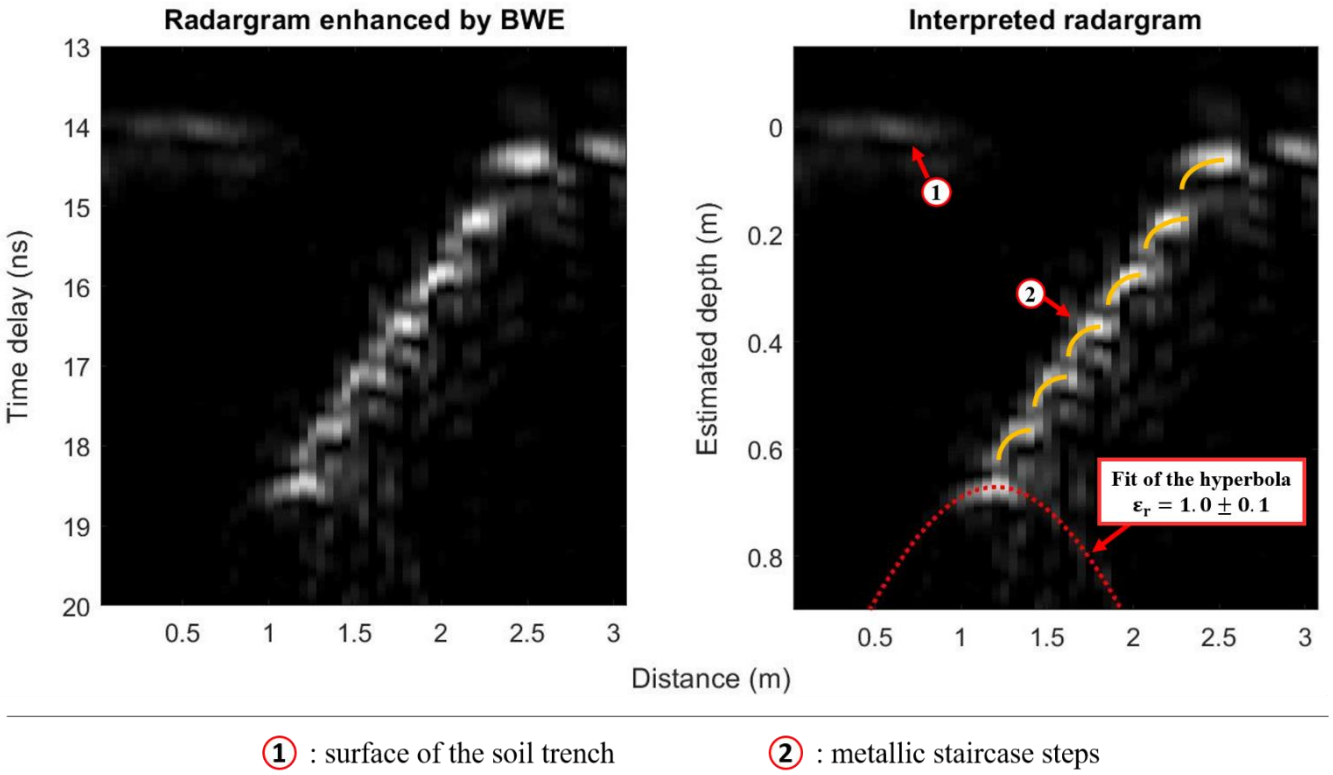

Figure 15: TUD "staircase" radargram after BWE (a) and its interpretation (b)

6.2. Icy environments: The Chamonix and the Dachstein Giant Ice Cave campaigns

When selecting a field test location for WISDOM, one must favour environments with as little liquid water as possible. Indeed, liquid water tends to increase absorption losses in the subsurface thus causing strong and rapid attenuation of the electromagnetic waves as they propagate. In contrast, water ice is a low-loss material at radar frequencies, and thus a favourable environment for GPR soundings. For these reasons, the two field campaigns presented here were performed in icy environments (Figure 16). Even if no evidence of underground water ice at Oxia Planum have been reported so far, and even if the latitude of the landing site is too close to the equator to sustain stable water ice in its shallow subsurface (Mellon and Jakosky, 1993), remnants of ground water ice (Clifford and Hillel, 1983; Forget et al., 2006) in equatorial regions is a

possibility. Wilson et al. (2018) for instance presents observations consistent with the presence of such remnants or, alternatively, hydrated minerals, in other equatorial regions.

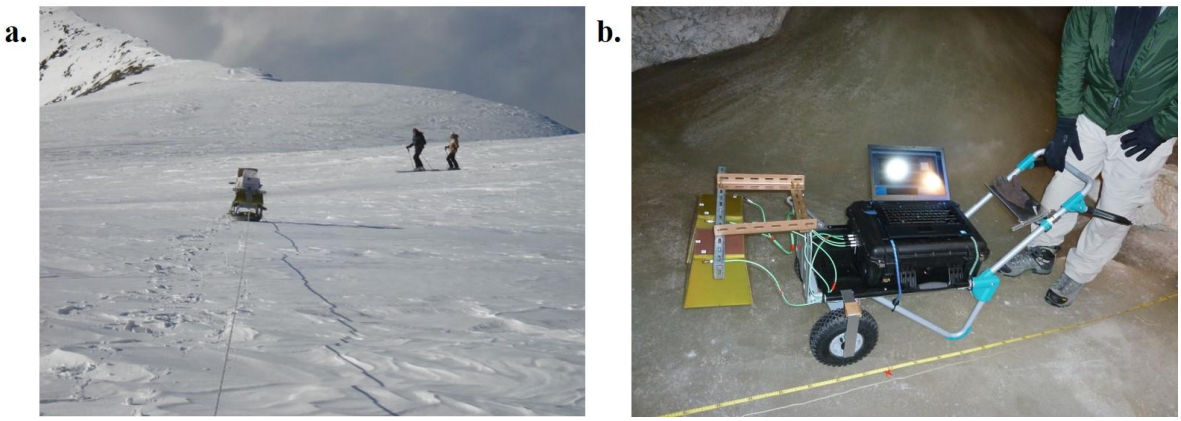

Figure 16: Illustrations of the icy-environments WISDOM field campaigns a. The Chamonix campaign (France) b. The Dachstein Giant Ice Caves (Austria)

6.2.1. The Chamonix campaign

The first WISDOM campaign performed in an icy environment took place in Chamonix (French Alps) in winter 2011. To ease the movements of the instrument in this snowy environment, a prototype version of WISDOM was mounted on a sledge.

The radargram presented in Figure 17 has been acquired in the Grands Montets region (Vallée Blanche), and clearly shows three different layered underground structures. Note that layered structures (though lithic ones) are also expected on Oxia Planum, the ExoMars future landing site, as a result of a fan sediment deposition (Quantin-Nataf et al., 2019). Figure 17 shows clear improvement in resolution after BWE which leads to a better separation and therefore detection of the layers. New details even appear in some regions of the radargram (see green arrows in Figure 17.b).

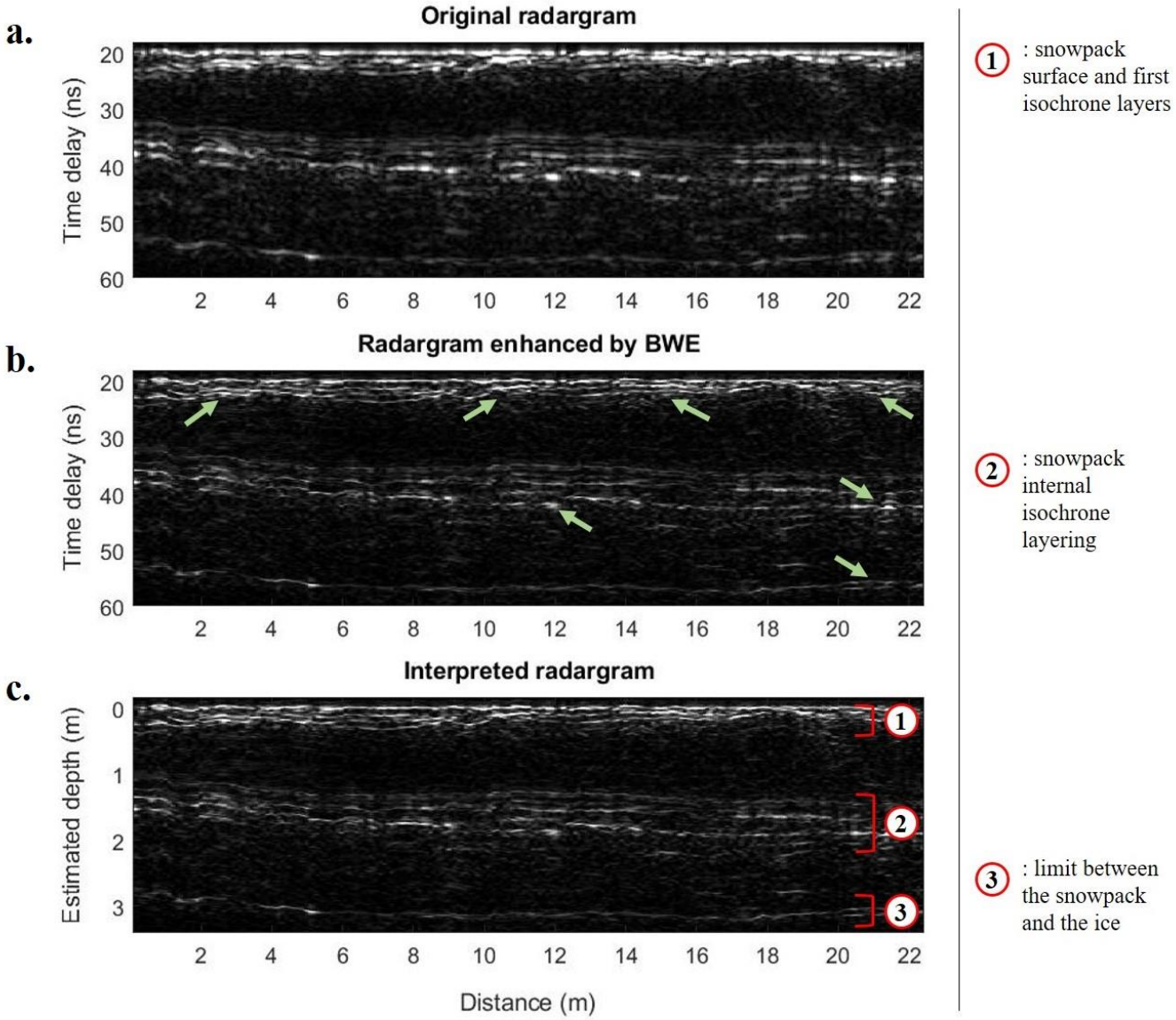

Figure 17: Radargram from the Chamonix field campaign, before (a) and after (b) application of the BWE. Panel (c) proposes interpretation. The time delays have been converted into distance assuming a dielectric constant of 3.1.

To obtain an estimation of depth in the radargram from the measured time delays, a dielectric constant of 3.1 (close to the dielectric constant of water ice at GHz frequencies) has been assumed. Close to the surface, in the uppermost subsurface layer, ~10 cm thick isochrone layers of snow can be observed. They likely correspond to recent precipitation (snow fall) events. A snowpack internal layering can be observed around a depth of 1.5 m, likely corresponding to older precipitation events, and possibly to the separation between snow layers and névé layers. The interface, at a depth around 3 m, may indicate the limit between the snowpack and the ice of the glacier. Beneath this last interface, no evidence of structure is visible suggesting that the

compacted ice below is homogeneous at spatial scale of the order of a ~5 cm. Such a 3-layer structure of the snowpack is not unusual, and is for instance also visible in radargrams acquired by Gusmeroli et al. (2014) on the snowpack of the Scott Glacier, in Alaska.

6.2.2 The Dachstein Giant Ice Cave campaign

The second WISDOM campaign on an icy environment took place in the Dachstein Giant Ice Cave (Austria), in April 2012 and was part of the *Dachstein Mars Simulation* campaign organised by the Austrian Space Forum (Groemer et al., 2012). Figure 18 displays the radargram acquired in this cave before and after BWE; different buried structures of interest can be identified, such as layering in the ice sheet, the bedrock below and trapped boulders in between. Similar structures will be hunt down in the subsurface of Oxia Planum, on Mars (Vago et al., 2017).

At depths of 0.6 - 1.2 m, the ice-sheet exhibits a layered structure (yellow lines in Figure 18.c). In a previous study, Dorizon et al. (2016) estimate the thickness of Dachstein ice layers to range from a few cm to 10 cm. The resolution of WISDOM in pure water ice after windowing being ~6 cm, these underground structures are particularly enhanced after application of the BWE and a new layer is even revealed (green arrow in Figure 18.b). While segregated ice is not expected in abundance in Oxia Planum, layered structure related to sedimentary deposits may be present in this region which is rich in clay-bearing units (Quantin-Nataf et al., 2019).

Hyperbolic patterns corresponding to echoes generated by rocks beneath the ice-sheet can be observed at depths 0.4 - 2 m. After application of the BWE, they are more readily located and can be used with more confidence to derive the dielectric constant of their surrounding medium. We recall that, in the frame of the ExoMars mission, hyperbolic patterns indicating the likely presence of buried rocks will be regions to avoid for the safety of the drill.

On the contrary, the underground continuation of surface outcrops will be a favored target for the drill of the Rosalind Franklin rover. In that regard, as another gain of BWE, the echoes from the bedrock beneath the ice-sheet of the Dachstein can be observed in much greater details after application of this technique (blue lines in Figure 18.c). They reveal 2 underground rough interfaces that seem to be interrupted at a distance of ~5.5m

620 unless they form a continuous bedrock exhibiting a very steep slope in this area which would make it invisible
621 to WISDOM (Ciarletti et al., 2017).

622

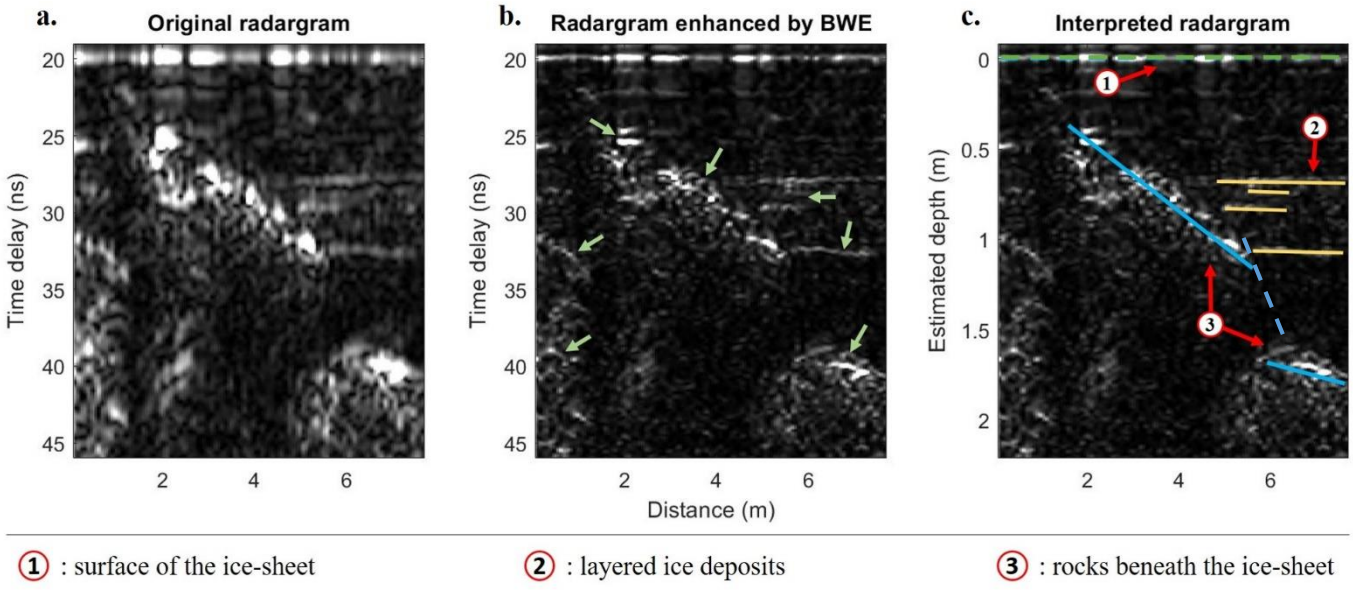

623

624 *Figure 18: Radargram from the Dachstein field campaign before (a) and after (b,c) application of the*
625 *BWE. In (b) the green arrows point to details of the scattering structures that where not resolved before*
626 *application of the BWE. In (c) time delays have been converted into distance assuming a dielectric constant*
627 *of 3.1 and structures of interest are indicated.*

628 The radargrams from both campaigns in icy environments have shown the value of the BWE technique in
629 terms of resolution and interpretation enhancement. However, as mentioned above, icy environments are very
630 favourable to radio wave propagation and it is important to also demonstrate the ability of the BWE to improve
631 WISDOM scientific return in dry, but more lossy, lithic environments that is, environments likely more
632 analogous to the region that will be explored by the ExoMars rover.

633 **6.3 Lithic environment: The Etna campaign**

634

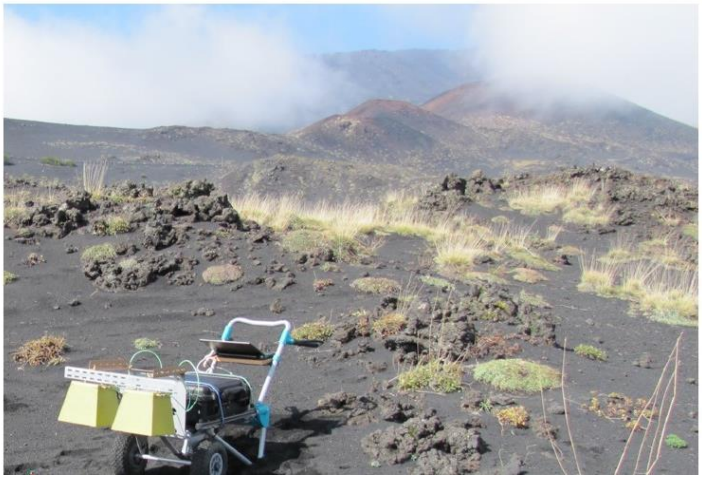

Figure 19: WISDOM on the flank of the Etna volcano

In 2010, a prototype model of the WISDOM instrument was brought to a volcanic site in the Etna mountain region (see Figure 19), in Sicily (Italy). Some results of this field test are shown in Ciarletti et al. (2017). Such an environment may be a good analog for Oxia Planum, where likely volcanic "dark resistant units" are exposed at the surface (Quantin-Nataf et al., 2019). Though is it not a primary objective of the mission, volcanic terrains will be most likely investigated by WISDOM on Mars.

The radargram shown in Figure 20 has been selected because it displays different subsurface deposit layers corresponding to at least two different volcanic events. Even if WISDOM penetration depth is, as expected, smaller than in icy environments due to higher losses (< 1 m against 2-3 m), several layers can be clearly identified and are better separated after the application of the BWE (yellow lines in Figure 20.c) while some deep structures appear clearer (blue lines Figure 20.c), and small details are revealed (green arrows in Figure 20.b).

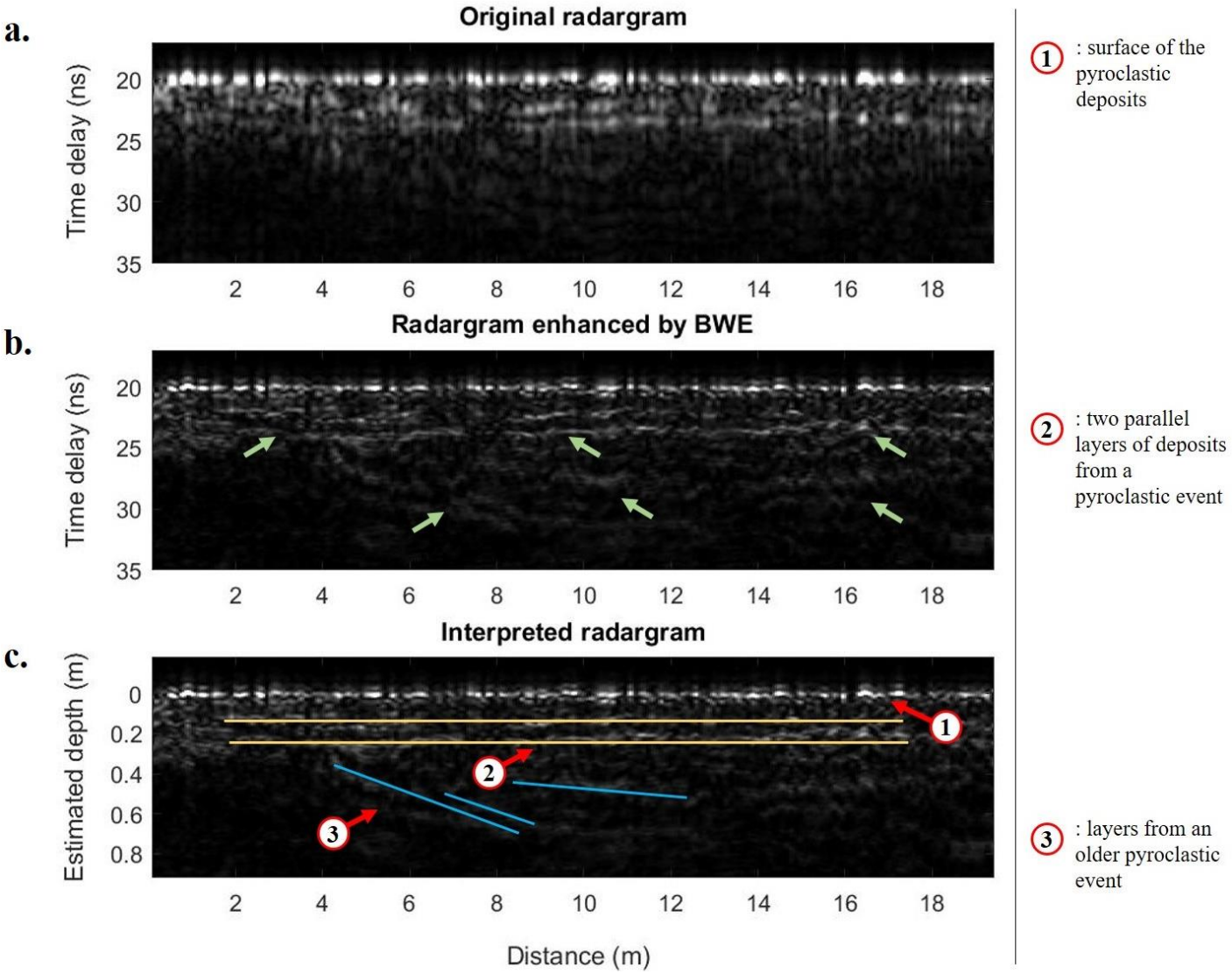

Figure 20: Radargram from the Etna field campaign before (a) and after (b, c) application of the BWE. In (b) the green arrows point to details of the scattering structures that where not resolved before application of the BWE. In (c) time delays have been converted into distance assuming a dielectric constant of 6 (as derived from the surface echo amplitude) and structures of interest are indicated

More specifically, 2 highly reflective layers, parallel to the surface, can be observed between 20 and 30 cm of depth (yellow lines in Figure 20.c); they probably originate from the same pyroclastic event. Beneath these two layers, tilted interfaces are detected (in blue). They have been previously interpreted as deposits from an older pyroclastic event (Ciarletti et al., 2017). The material from these two events is superimposed over distances inferior to 4 m.

As a conclusion, the application of the BWE technique to WISDOM radargram proves to be very valuable even on a lithic environment which is promising for future operations Mars.

7. Conclusions and Perspectives

In the present study we have adapted and applied for the first time to WISDOM data the super-resolution method known as "Bandwidth Extrapolation technique". While the technique has already been successfully applied to observations from planetary orbital radar sounders (MARSIS/Mars Express, SHARAD/MRO, Cassini radar), this is, to our knowledge, its first application to planetary surface GPR soundings. The BWE technique is now implemented in the WISDOM processing pipeline described in Hervé et al. (2020).

As the WISDOM instrument is set to arrive on Mars only in 2023, the BWE has been methodologically tested on synthetic, experimental and field test data. We have demonstrated its ability to improve the vertical resolution of WISDOM radargrams by a factor of 3, while preserving useful information on the distance and amplitude of the detected echoes. The value of the BWE has been shown on radargrams acquired in both icy and lithic (and therefore more lossy) natural environments. The detection of subsurface structures of interest such as layering or hyperbolic scattering patterns is clearly eased by the BWE and the interpretation of WISDOM radargrams facilitated. These are promising results for future operations on Mars.

Once on Mars, the improvement in vertical resolution of WISDOM radargrams, and therefore the improved separation of echoes from underground reflectors, will indeed be essential to ensure the drill safety by avoiding buried rocks as well as to investigate of the geological history of the ExoMars landing site, Oxia Planum. At least two layered clay-bearing units have been identified in this site (Quantin-Nataf et al., 2019), and we have shown in this study the ability of the BWE to ease the interpretation of a layered subsurface. The synergy between WISDOM and other instruments of the Rosalind Franklin rover payload will also be enhanced thanks to super-resolved radargrams. In particular, a finer knowledge of the stratigraphy below the rover will benefit to the Ma_MISS instrument (the visible and near-IR spectrometer mounted on the rover drill) (De Sanctis et al., 2017) which will analyse the subsurface composition during drilling operations. Information on the layers

683 detected by WISDOM will indeed be associated with the ones detected by Ma_Miss. Likewise, a better
684 resolved surface echo will ease the comparison to PanCam (panoramic camera of the rover) (Coates et al.,
685 2017) images.

686 The BWE technique presented here can be further improved using the different polarization channels of
687 WISDOM. Indeed, the instrument has the capacity to transmit and receive in two polarizations, resulting into
688 four polarization channels. A polarimetric version of the BWE, as implemented by Suwa and Iwamoto (2007),
689 would improve the reconstruction of echoes detected on different polarization channels. Another perspective
690 of improvement could result from accounting for the high-frequencies decay in a lossy medium when
691 extrapolating the bandwidth of the instrument, as well as for white noise as proposed by Piou et al. (1999).
692 The application of these lines of improvement to WISDOM radargrams is currently under investigation.

693 As previously mentioned, WISDOM will not be the only Ground Penetrating Radar to operate on the Martian
694 surface in the next few years. But with its large bandwidth, and the implementation of the super-resolution
695 technique evaluated in this study, the ExoMars mission will provide the radargrams with the highest vertical
696 resolution ever acquired on Mars, providing unique insights into the Martian shallow subsurface.

697

698 Acknowledgements

699

700 Development of the WISDOM instrument and preparation of the data processing and interpretation have been
701 funded and supported by CNES (Centre National d'Etudes Spatiales, France) and DLR (Deutsches Zentrum
702 für Luft- und Raumfahrt, Germany). Nicolas Oudart's PhD fellowship is funded by CNES and UVSQ
703 (Université de Versailles Saint-Quentin). We would like to thank David Stillman (Southwest Research
704 Institute) for his comments which improved this article.

705

706 References

707

Bowling, S.B., 1977. Linear Prediction and Maximum Entropy Spectral Analysis for Radar Applications. Proj. Rep. RMP-122, MIT Lincoln Lab.

Brouet, Y., Becerra, P., Sabouroux, P., Pommerol, A., Thomas, N., 2019. A laboratory-based dielectric model for the radar sounding of the martian subsurface. Icarus 321, 960–973. https://doi.org/10.1016/j.icarus.2018.12.029

Burg, J.P., 1967. Maximum Entropy Spectral Analysis. 37th Meet. Soc. Explor. Geophys.

Capineri, L., Grande, P., Temple, J.A.G., 1998. Advanced image-processing technique for real-time interpretation of ground-penetrating radar images. Int. J. Imaging Syst. Technol. 9, 51–59. https://doi.org/10.1002/(SICI)1098-1098(1998)9:1<51::AID-IMA7>3.0.CO;2-Q

Ciarletti, V., 2016. A variety of radars designed to explore the hidden structures and properties of the Solar System's planets and bodies. Comptes Rendus Phys. https://doi.org/10.1016/j.crhy.2016.07.022

Ciarletti, V., Clifford, S., Plettemeier, D., Le Gall, A., Hervé, Y., Dorizon, S., Quantin-Nataf, C., Benedix, W.S., Schwenzer, S., Pettinelli, E., Heggy, E., Herique, A., Berthelier, J.J., Kofman, W., Vago, J.L., Hamran, S.E., 2017. The WISDOM Radar: Unveiling the Subsurface Beneath the ExoMars Rover and Identifying the Best Locations for Drilling. Astrobiology 17, 565–584. https://doi.org/10.1089/ast.2016.1532

Ciarletti, V., Corbel, C., Plettemeier, D., Caïs, P., Clifford, S.M., Hamran, S.E., 2011. WISDOM GPR Designed for shallow and high-resolution sounding of the martian subsurface, in: Proceedings of the IEEE. pp. 824–836. https://doi.org/10.1109/JPROC.2010.2100790

Clifford, S.M., Hillel, D., 1983. The stability of ground ice in the equatorial region of Mars. J. Geophys. Res. 88, 2456. https://doi.org/10.1029/jb088ib03p02456

Coates, A.J., Jaumann, R., Griffiths, A.D., Leff, C.E., Schmitz, N., Josset, J.L., Paar, G., Gunn, M., Hauber, E., Cousins, C.R., Cross, R.E., Grindrod, P., Bridges, J.C., Balme, M., Gupta, S., Crawford, I.A., Irwin, P., Stabbins, R., Tirsch, D., Vago, J.L., Theodorou, T., Caballo-Perucha, M., Osinski, G.R., 2017. The PanCam Instrument for the ExoMars Rover. Astrobiology 17, 511–541.

https://doi.org/10.1089/ast.2016.1548

Cuomo, K.M., 1992. A Bandwidth Extrapolation Technique for Improved Range Resolution of Coherent Radar Data, Lincoln Laboratory Report.

Daniels, D.J., 2005. Ground Penetrating Radar, in: IET (Ed.), Encyclopedia of RF and Microwave Engineering. John Wiley & Sons, Inc., Hoboken, NJ, USA. https://doi.org/10.1002/0471654507.eme152

De Sanctis, M.C., Altieri, F., Ammannito, E., Biondi, D., De Angelis, S., Meini, M., Mondello, G., Novi, S., Paolinetti, R., Soldani, M., Mugnuolo, R., Pirrotta, S., Vago, J.L., the Ma_MISS team, 2017. Ma_MISS on ExoMars: Mineralogical Characterization of the Martian Subsurface. Astrobiology 17, 612–620. https://doi.org/10.1089/ast.2016.1541

Dorizon, S., Ciarletti, V., Plettemeier, D., Benedix, W.S., 2016. Performance validation of the ExoMars 2018 WISDOM GPR in ice caves, Austria. Planet. Space Sci. 120, 1–14. https://doi.org/10.1016/j.pss.2015.10.008

Elachi, C., Allison, M.D., Borgarelli, L., Encrenaz, P., Im, E., Janssen, M.A., Johnson, W.T.K., Kirk, R.L., Lorenz, R.D., Lunine, J.I., Muhleman, D.O., Ostro, S.J., Picardi, G., Posa, F., Rapley, C.G., Roth, L.E., Seu, R., Soderblom, L.A., Vetrella, S., Wall, S.D., Wood, C.A., Zebker, H.A., 2005. Radar: The Cassini Titan RADAR mapper. Space Sci. Rev. https://doi.org/10.1007/s11214-004-1438-9

Fang, G., Zhou, B., Ji, YC, Q.Z., 2014. Lunar Penetrating Radar onboard the Chang'e-3 mission. iopscience.iop.org.

Forget, F., Haberle, K.M., Montmessin, F., Levrard, B., Head, J.W., 2006. Formation of glaciers on Mars by atmospheric precipitation at high obliquity. Science (80-.). 311, 368–371. https://doi.org/10.1126/science.1120335

Groemer, G., Luger, U., Juhart, K., Plettemeier, D., Hettrich, S., Sans, A., Souchier, A., Vimercati, L., Noell, A., Boehme, R., Balwant, R., Rodrigues, L., Mogosanu, H., Carbognani, F., Meszyński, S., 2012. (PDF) Dachstein Mars Simulation 2012 Mission Report [WWW Document]. URL

https://www.researchgate.net/publication/235753475_Dachstein_Mars_Simulation_2012Mission_Report (accessed 7.30.20).

Gusmeroli, A., Wolken, G.J., Arendt, A.A., 2014. Helicopter-borne radar imaging of snow cover on and around glaciers in Alaska. Ann. Glaciol. 55, 78–88. https://doi.org/10.3189/2014AoG67A029

Hamran, S.E., Amundsen, H.E.F., Carter, L.M., Ghent, R.R., Kohler, J., Mellon, M.T., Paige, D.A., 2014. The RIMFAX Ground Penetrating Radar on the Mars 2020 Rover, in: AGU Fall Meeting Abstracts. p. 3746.

Hassler, D.M., Zeitlin, C., Wimmer-Schweingruber, R.F., Ehresmann, B., Rafkin, S., Eigenbrode, J.L., Brinza, D.E., Weigle, G., Böttcher, S., Böhm, E., Burmeister, S., Guo, J., Köhler, J., Martin, C., Reitz, G., Cucinotta, F.A., Kim, M.H., Grinspoon, D., Bullock, M.A., Posner, A., Gómez-Elvira, J., Vasavada, A., Grotzinger, J.P., 2014. Mars' surface radiation environment measured with the Mars science laboratory's curiosity rover. Science (80-.). 343. https://doi.org/10.1126/science.1244797

Hervé, Y., Ciarletti, V., Le Gall, A., Corbel, C., Hassen-Khodja, R., Benedix, W.S., Plettemeier, D., Humeau, O., Vieau, A.J., Lustrement, B., Abbaki, S., Bertran, E., Lapauw, L., Tranier, V., Oudart, N., Vivat, F., Statz, C., Lu, Y., Hegler, S., Hérique, A., 2020. The WISDOM radar on board the ExoMars 2020 Rover: Characterization and calibration of the flight model. Planet. Space Sci. 104939. https://doi.org/10.1016/j.pss.2020.104939

Kay, S.M., Marple, S.L., 1981. Spectrum Analysis—A Modern Perspective. Proc. IEEE 69, 1380–1419. https://doi.org/10.1109/PROC.1981.12184

Kobayashi, T., Kim, J.H., Lee, S.R., Kumamoto, A., Nakagawa, H., Oshigami, S., Oya, H., Yamaguchi, Y., Yamaji, A., Ono, T., 2012. Synthetic aperture radar processing of Kaguya lunar radar sounder data for lunar subsurface imaging. IEEE Trans. Geosci. Remote Sens. 50, 2161–2174. https://doi.org/10.1109/TGRS.2011.2171349

Kofman, W., Barbin, Y., Klinger, J., Levasseur-Regourd, A.C., Barriot, J.P., Hérique, A., Hagfors, T., Nielsen, E., Grün, E., Edenhofer, P., Kochan, H., Picardi, G., Seu, R., Van Zyl, J., Elachi, C., Melosh,

J., Veverka, J., Weissman, P., Svedhem, L.H., Hamran, S.E., Williams, I.P., 1998. Comet nucleus sounding experiment by radiowave transmission. Adv. Sp. Res. 21, 1589–1598. https://doi.org/10.1016/S0273-1177(97)00952-6

Magnani, P., Re, E., Senese, S., Rizzi, F., Gily, A., Baglioni, P., 2010. The Drill and Sampling System for the ExoMars Rover 222–228.

Mastrogiuseppe, M., Poggiali, V., Hayes, A., Lorenz, R., Lunine, J., Picardi, G., Seu, R., Flamini, E., Mitri, G., Notarnicola, C., Paillou, P., Zebker, H., 2014. The bathymetry of a Titan sea. Geophys. Res. Lett. 41, 1432–1437. https://doi.org/10.1002/2013GL058618

Mellon, M.T., Jakosky, B.M., 1993. Geographic variations in the thermal and diffusive stability of ground ice on Mars. J. Geophys. Res. 98, 3345–3364. https://doi.org/10.1029/92JE02355

Mitrofanov, I.G., Litvak, M.L., Nikiforov, S.Y., Jun, I., Bobrovnitsky, Y.I., Golovin, D. V, Grebennikov, A.S., Fedosov, F.S., Kozyrev, A.S., Lisov, D.I., Malakhov, A. V, Mokrousov, M.I., Sanin, A.B., Shvetsov, V.N., Timoshenko, G.N., Tomilina, T.M., Tret'Yakov, V.I., Vostrukhin, A.A., 2017. The ADRON-RM Instrument Onboard the ExoMars Rover. Astrobiology. https://doi.org/10.1089/ast.2016.1566

Moore, T., Zuerndorfer, B., Burt, E., 1997. Enhanced Imagery Using Spectral-Estimation-Based Techniques. Lincoln Lab. J. 10, 171–186.

National Instruments Inc., 2009. The Fundamentals of FFT-Based Signal Analysis and Measurement in LabVIEW and LabWindows / CVI [WWW Document]. Natl. Instruments White Pap. URL www.ni.com/white-paper/4278/en/ (accessed 6.22.20).

Picardi, G., Biccari, D., Cartacci, M., Cicchetti, A., Giuppi, S., Marini, A., Masdea, A., Noschese, R., Piccari, F., Seu, R., Plaut, J.J., Johnson, W.T.K., Jordan, R.L., Safaeinili, A., Federico, C., Frigeri, A., Melacci, P.T., Orosei, R., Bombaci, O., Calabrese, D., Zampolini, E., Edenhofer, P., Plettemeier, D., Marinangeli, L., Pettinelli, E., Hagfors, T., Flamini, E., Vannaroni, G., Nielsen, E., Williams, I., Gurnett, D.A., Kirchner, D.L., Huff, R.L., 2008. Marsis data inversion approach: Preliminary results,

in: 2008 IEEE Radar Conference, RADAR 2008. https://doi.org/10.1109/RADAR.2008.4721073

Picardi, G., Plaut, J.J., Biccari, D., Bombaci, O., Calabrese, D., Cartacci, M., Cicchetti, A., Clifford, S.M., Edenhofer, P., Farrell, W.M., Federico, C., Frigeri, A., Gurnett, D.A., Hagfors, T., Heggy, E., Herique, A., Huff, R.L., Ivanov, A.B., Johnson, W.T.K., Jordan, R.L., Kirchner, D.L., Kofman, W., Leuschen, C.J., Nielsen, E., Orosei, R., Pettinelli, E., Phillips, R.J., Plettemeier, D., Safaeinili, A., Seu, R., Stofan, E.R., Vannaroni, G., Watters, T.R., Zampolini, E., 2005. Planetary science: Radar soundings of the subsurface of Mars. Science (80-.). 310, 1925–1928. https://doi.org/10.1126/science.1122165

Piou, J., Cuomo, K., Mayhan, J., 1999. A State-Space Technique for Ultrawide-Bandwidth Coherent Processing. Proj. Rep. 1054, MIT Lincoln Lab.

Plettemeier, D., Ciarletti, V., Hamran, S.E., Corbel, C., Cais, P., Benedix, W.S., Wolf, K., Linke, S., Röddecke, S., 2009. Full polarimetric GPR antenna system aboard the ExoMars rover, in: IEEE National Radar Conference - Proceedings. https://doi.org/10.1109/RADAR.2009.4977120

Quantin-Nataf, C., Carter, J., Mandon, L., Balme, M., Fawdon, P., Davis, J., Thollot, P., Dehouck, E., Pan, L., Volat, M., Millot, C., Breton, S., Loizeau, D., Vago, J.L., 2019. ExoMars at Oxia Planum, Probing the aqueous-related Noachian environments. Ninth Int. Conf. Mars 2019 2089.

Raguso, M.C., 2018. Sounder Data Processing and Techniques for Geophysical Parameters Estimation. La Sapienza Univ. PhD thesis.

Raguso, M.C., Piazzo, L., Mastrogiuseppe, M., Seu, R., Orosei, R., 2018. Resolution enhancement and interference suppression for planetary radar sounders, in: European Signal Processing Conference. pp. 1212–1216. https://doi.org/10.23919/EUSIPCO.2018.8553468

Seu, R., Biccari, D., Orosei, R., Lorenzoni, L. V., Phillips, R.J., Marinangeli, L., Picardi, G., Masdea, A., Zampolini, E., 2004. SHARAD: The MRO 2005 shallow radar, in: Planetary and Space Science. pp. 157–166. https://doi.org/10.1016/j.pss.2003.08.024

Suwa, K., Iwamoto, M., 2007. A two-dimensional bandwidth extrapolation technique for polarimetric synthetic aperture radar images. IEEE Trans. Geosci. Remote Sens. 45, 45–54.

https://doi.org/10.1109/TGRS.2006.885406

Vago, J.L., Westall, F., Coates, A.J., Jaumann, R., Korablev, O., Ciarletti, V., Mitrofanov, I., Josset, J.L., De Sanctis, M.C., Bibring, J.P., Rull, F., Goesmann, F., Steininger, H., Goetz, W., Brinckerhoff, W., Szopa, C., Raulin, F., Edwards, H.G.M., Whyte, L.G., Fairén, A.G., Bridges, J., Hauber, E., Ori, G.G., Werner, S., Loizeau, D., Kuzmin, R.O., Williams, R.M.E., Flahaut, J., Forget, F., Rodionov, D., Svedhem, H., Sefton-Nash, E., Kminek, G., Lorenzoni, L., Joudrier, L., Mikhailov, V., Zashchirinskiy, A., Alexashkin, S., Calantropio, F., Merlo, A., Poulakis, P., Witasse, O., Bayle, O., Bayón, S., Meierhenrich, U., Carter, J., García-Ruiz, J.M., Baglioni, P., Haldemann, A., Ball, A.J., Debus, A., Lindner, R., Haessig, F., Monteiro, D., Trautner, R., Voland, C., Rebeyre, P., Goulty, D., Didot, F., Durrant, S., Zekri, E., Koschny, D., Toni, A., Visentin, G., Zwick, M., Van Winnendael, M., Azkarate, M., Carreau, C., 2017. Habitability on Early Mars and the Search for Biosignatures with the ExoMars Rover. Astrobiology. https://doi.org/10.1089/ast.2016.1533

Wilson, J.T., Eke, V.R., Massey, R.J., Elphic, R.C., Feldman, W.C., Maurice, S., Teodoro, L.F.A., 2018. Equatorial locations of water on Mars: Improved resolution maps based on Mars Odyssey Neutron Spectrometer data. Icarus 299, 148–160. https://doi.org/10.1016/j.icarus.2017.07.028

Yann Hervé; Valerie Ciarletti; Alice Le Gall; Charlotte Corbel; Rafik Hassen-Khodja; Wolf-Stefan Benedix; Dirk Plettemeier; Olivier Humeau; André-Jean Vieau; Benjamin Lustrement; Sadok Abbaki; Emmanuel Bertran; Laurent Lapauw; Vivien Tranier, N.O.A.H., 2020. The WISDOM radar on board the ExoMars 2020 Rover: Characterization and calibration of the flight model. Planet. Space Sci.

Zhan, X., Jiang, Z., Chen, Z., Zhang, M., Song, C., 2014. Performance evaluation of lunar penetrating radar onboard the rover of CE-3 probe based on results from ground experiments. Res. Astron. Astrophys. 14, 433–455. https://doi.org/10.1088/1674

Zhou, B., Shen, S.X., Ji, Y.C., Lu, W., Zhang, F., Fang, G.Y., Su, Y., Dai, S., 2016. The subsurface penetrating radar on the rover of China's Mars 2020 mission, in: Proceedings of 2016 16th International Conference of Ground Penetrating Radar, GPR 2016. Institute of Electrical and Electronics Engineers Inc. https://doi.org/10.1109/ICGPR.2016.7572700

859